Journal of Catalysis 333 (2016) 184–199

Contents lists available at ScienceDirect

Journal of Catalysis

journal homepage: www.elsevier.com/locate/jcat

Efficient conversion of levulinic acid or furfuryl alcohol into alkyl levulinates catalyzed by heteropoly acid and ZrO_2 bifunctionalized organosilica nanotubes

Daiyu Song [b], Sai An [b], Yingnan Sun [a], Yihang Guo [a,*]

[a] School of Environment, Northeast Normal University, Changchun 130117, People's Republic of China
[b] School of Chemistry, Northeast Normal University, Changchun 130024, People's Republic of China

ARTICLE INFO

Article history:
Received 6 August 2015
Revised 22 October 2015
Accepted 24 October 2015

Keywords:
Alkyl levulinate
Biomass-derived platform molecule
Solid acid
Hollow nanotube
Organic–inorganic hybrid catalyst

ABSTRACT

A series of heteropoly acid and ZrO_2 bifunctionalized organosilica nanotubes (PW_{12}/ZrO_2-Si(Et)Si-NTs) were fabricated via a P123 single-micelle-templated sol–gel co-condensation route and carefully adjusted Si-to-Zr molar ratio and acidity in the initial gel mixture. The morphological characteristics, textural properties, Brønsted and Lewis acidity, and structural integrity of the incorporated Keggin units, as well as the formation of the carbon/silica framework, were well characterized. The PW_{12}/ZrO_2-Si(Et)Si-NTs hybrid nanocatalysts were applied in the synthesis of alkyl levulinates by esterification of levulinic acid and ethanolysis of furfuryl alcohol, and the obtained excellent catalytic activity was explained in terms of the strong Brønsted and Lewis acidity, unique hollow tubular nanostructure, and hydrophobic surface of the hybrid nanocatalysts; additionally, the catalysts could be reused at least three times without significant loss of activity. Finally, the possible reaction mechanism of the PW_{12}/ZrO_2-Si(Et)Si-NTs-catalyzed esterification and ethanolysis reactions were put forward.

1. Introduction

The design and development of organic–inorganic hybrid nanocatalysts for the transformation of biomass into biofuels and value-added chemicals is an important area in green and sustainable chemistry [1,2]. With unique textural properties, interesting morphologies, and multifunctionality, the hybrid nanocatalysts generally possess outstanding advantages including plentiful active sites, low diffusion and mass transfer resistance, and tunable surface hydrophobicity/hydrophilicity, which eventually facilitate the access of the substrates to the active sites. Currently, hybrid nanocatalysts with various nanostructures such as nanospheres, nanowires, nanotubes, nanorods, and nanopores have emerged as powerful tools for the efficient conversion of raw materials into useful chemicals [3–9]. Among them, spherical and tubular hybrid nanocatalysts with hollow interiors, permeable and thin shells (thickness of several nanometers), nanometric size (diameter of several tens of nanometers), thermal and mechanical stability, decreased mass-transfer distance, and hierarchical pore structure have attracted particular interest, and they allow most of the active sites to be confined inside the spheres or tubes, serving as nanoreactors for various organic transformations [10]. For example, organosulfonic acid-functionalized silica materials represent attractive alternatives to the hazardous homogeneous acid catalysts, and they have been widely applied in a variety of organic transformations including the synthesis of biofuel and chemicals from biomass feedstocks [11–15]. Previous studies indicated that organosulfonic acid-functionalized alkyl-bridged organosilica nanotubes or nanospheres exhibited higher catalytic activity than their bulk mesoporous counterparts in biomass-conversion-related esterification, transesterification, or ethanolysis reactions [16–18]. Similar results were also observed in heteropoly acids (HPAs) and ZrO_2-bifunctionalized organosilica hollow nanosphere ($H_3PW_{12}O_{40}/ZrO_2$-*Et*-HNS)-catalyzed esterification and transesterification reactions, and the $H_3PW_{12}O_{40}/ZrO_2$-*Et*-HNS exhibited higher acid catalytic activity than their periodic mesoporous counterparts [19].

To further the development of robust, multifunctional, and recoverable HPA-based organic–inorganic hybrid nanocatalysts, in the present work, both Keggin-type HPA ($H_3PW_{12}O_{40}$) and ZrO_2-bifunctionalized organosilica nanotubes (PW_{12}/ZrO_2-Si(Et)Si-NTs) were successfully fabricated via a carefully designed P123 single-micelle-templated sol–gel co-condensation route. The procedure included one-step co-condensation of bridging organosilane (1,2-bis(trimethoxysilyl)ethane) and zirconium

* Corresponding author. Fax: +86 431 89165626.
E-mail address: guoyh@nenu.edu.cn (Y. Guo).

http://dx.doi.org/10.1016/j.jcat.2015.10.018
0021-9517/

n-butoxide around P123 polymer micelles in the presence of $H_3PW_{12}O_{40}$. HPAs such as Keggin (e.g., $H_3PW_{12}O_{40}$) and Dawson acids (e.g., $H_6P_2W_{18}O_{62}$) are seen as environmentally benign and economically feasible alternatives to conventional acid catalysts because of their superstrong Brønsted acidity, high proton mobility, and stability, and they exhibit excellent catalytic behavior in a wide variety of acid-catalyzed organic transformations [20,21]. However, HPAs are soluble in polar media that make their recovery difficult [22]; additionally, BET surface areas of bulk HPAs are very small (lower than 5 $m^2\ g^{-1}$), which lead to poor access to the active sites [23,24]. These disadvantages can be overcome by dispersing them within various porous materials [22–24]. ZrO_2 possesses both Brønsted and Lewis acidity [25,26], and the Brønsted acidity of the Keggin units and ZrO_2 is further enhanced by strong W—O—Zr covalent bindings between $H_3PW_{12}O_{40}$ clusters and the ZrO_2 support [19,27–30]. Meanwhile, the strong interaction between $H_3PW_{12}O_{40}$ and ZrO_2 can effectively inhibit $H_3PW_{12}O_{40}$ leaching, which generally occurs in most of the supported HPA catalyst systems, leading to prepared PW_{12}/ZrO_2-Si(Et)Si-NTs sufficiently robust to survive under harsh reaction conditions (e.g., hydrothermal or solvothermal treatment) and simultaneously minimize the leaching of the Keggin units in polar media. On the other hand, incorporation of the hydrophobic organosilica moieties (e.g., bridging ethyl groups) throughout the PW_{12}/ZrO_2 framework can rationally adjust the textural properties and surface hydrophobicity/hydrophilicity of the hybrid nanocatalysts, exerting a positive influence on the catalytic activity and stability of the hybrid nanocatalysts.

As-prepared PW_{12}/ZrO_2-Si(Et)Si-NTs hybrid nanocatalysts were applied in the synthesis of alkyl levulinates by esterification of levulinic acid and ethanolysis of furfuryl alcohol. For the esterification of levulinic acid, yielded water may poison the catalysts and decelerate the esterification reaction process; additionally, levulinic acid has a high cost as a raw material for this purpose. The development of inexpensive feedstock and a facile catalyst system to produce alkyl levulinates is therefore strongly demanded. Furfuryl alcohol, a lower-cost raw material, can be effectively used for the synthesis of alkyl levulinates by the alcoholysis reaction in the presence of acid catalysts. Alkyl levulinates such as methyl, ethyl, and *n*-butyl levulinate have found extensive applications in the flavoring and fragrance industry and as precursors to produce chemicals (e.g., γ-valerolactone) that can be converted to liquid alkanes and transportation fuels [21,31,32]. The threat of fossil oil shortage is stimulating the search for more sustainable fuel and chemical resources; accordingly, efficient conversion of further downstream acid hydrolysis products of biomass-derived C_5 or C_6 carbohydrates, e.g., levulinic acid or furfuryl alcohol, to alkyl levulinates attracts special interest [33]. On the other hand, it is imperative to develop green synthetic routes for alkyl levulinate production in order to meet the challenge of energy and sustainability, and replacement of hazardous liquid acid catalysts with solid acid catalysts is one of the effective strategies. By the combination of excellent morphological characteristics of tubes with hollow interiors, extremely small particle size, and thin tube thickness with strong Brønsted and Lewis acidity, as-prepared PW_{12}/ZrO_2-Si(Et)Si-NTs is expected to be a good candidate for alkyl levulinate production from biomass-derived platform molecules.

2. Experimental

2.1. Materials

$H_3PW_{12}O_{40}\cdot xH_2O$, Pluronic P123 ($EO_{20}PO_{70}EO_{20}$, M_w = 5800), 1,2-bis(trimethoxysilyl)ethane (BTMSE, 97%), zirconium *n*-butoxide [$Zr(OC_4H_9)_4$, 76–80% in *n*-butanol] and levulinic acid (98%) were purchased from Sigma–Aldrich. Furfuryl alcohol (98%) was purchased from Sinopharm Chemical Reagent Co., Ltd. 2-(Ethoxymethyl)furan (>95%) was purchased from Bide Pharmatech Ltd. Methyl levulinate (>99.0%), ethyl levulinate (>98.0%), and *n*-butyl levulinate (>98.0%) were purchased from TCI. Commercially available Amberlyst-15 was purchased from Alfa Aesar. These reagents were used without further purification.

2.2. Catalyst preparation

2.2.1. PW_{12}/ZrO_2-Si(Et)Si-NTs

Typically, P123 (0.45 g) was dissolved in HCl (1.9 mol L^{-1}, 15.6 g) at room temperature under stirring. The clear P123 solution was heated to 40 °C, and then BTMSE (0.6 mL) was added. Prehydrolysis of BTMSE for 45 min was applied prior to the addition of $Zr(OC_4H_9)_4$ (2.1 mL) to the mixture. After 1 h stirring, aqueous $H_3PW_{12}O_{40}$ (0.155 g in 2 mL water) was added dropwise to the solution. The resultant white suspension was stirred at 40 °C for 24 h. Subsequently, the suspension was transferred to an autoclave and heated at 100 °C with a heating rate of 2 °C min^{-1} for an additional 24 h. The resulting white solid powder was air-dried at 100 °C overnight, and then P123 in the product was removed by boiling ethanol washing and then air-dried at 100 °C for another 12 h. The initial molar ratio of the reactants is P123:$Zr(OC_4H_9)_4$:BTMSE:$H_3PW_{12}O_{40}$:HCl:H_2O = 0.0168:1:0.5:0.012:6:202. The product is denoted as *x*PW_{12}/ZrO_2-Si(Et)Si-NTs*y*, where *x* (wt.%) represents the determined $H_3PW_{12}O_{40}$ loading in the product (see Table 1), and *y* refers to initial Si-to-Zr molar ratio (here, *y* = 1.0).

Additionally, PW_{12}/ZrO_2-Si(Et)Si nanohybrids with initial Si-to-Zr molar ratios of 0.5, 0.75, 2.0, and 3.0 were prepared based on the above procedure but changing the $Zr(OC_4H_9)_4$-to-BTMSE molar ratio to 1:0.25, 1:0.375, 1:1, and 1:1.5, respectively.

2.2.2. PW_{12}/ZrO_2-Si(Et)Si-$2D_{hex}$

P123 (0.45 g) was dissolved in a mixture of water (14.2 mL) and HCl (12 mol L^{-1}, 0.8 mL) under vigorous stirring at room temperature. Subsequently, BTMSE (0.6 mL), $Zr(OC_4H_9)_4$ (2.1 mL), and aqueous $H_3PW_{12}O_{40}$ (0.155 g in 2 mL water) were added dropwise to the above solution at hourly intervals, successively. The resulting mixture was stirred at 40 °C for 24 h, and then it was transferred into an autoclave and placed into an oven. The oven was heated to 100 °C at a rate of 2 °C min^{-1} and then held for 24 h at 100 °C. The resulting white solid powder was air-dried at 100 °C overnight, and then P123 in the product was removed by boiling ethanol washing. The initial molar ratio of the reactants is P123:$Zr(OC_4H_9)_4$:BTMSE:$H_3PW_{12}O_{40}$:HCl:H_2O = 0.0168:1:0.5:0.012:2:202. The determined $H_3PW_{12}O_{40}$ loading in the product is 12.2 wt.% (see Table 1).

2.2.3. PW_{12}/ZrO_2-SiO_2-$2D_{hex}$

The procedure is similar to that of PW_{12}/ZrO_2-Si(Et)Si-NTs mentioned in Section 2.2.1 except for using TEOS (1 mL) as a silica precursor. The molar ratio of the reactants is P123:$Zr(OC_4H_9)_4$:TEOS:$H_3PW_{12}O_{40}$:HCl:H_2O = 0.0168:1:1:0.012:6:202. The determined $H_3PW_{12}O_{40}$ loading in the product is 12.1 wt.% (see Table 1).

2.2.4. PW_{12}/ZrO_2

The procedure is similar to that of the PW_{12}/ZrO_2-Si(Et)Si-NTs except that in the absence of BTMSE. The molar ratio of the reactants is P123:$Zr(OC_4H_9)_4$:$H_3PW_{12}O_{40}$:HCl:H_2O = 0.0168:2:0.012:6:202. The determined $H_3PW_{12}O_{40}$ loading in the product is 12.7 wt.% (see Table 1).

2.3. Catalyst characterization

TEM observations were performed on a JEM-2100F high-resolution transmission electron microscope at an accelerating

Table 1
Textural parameters and acid site density of various solid acid catalysts.

Entry	Catalyst	S_{BET} ($m^2\ g^{-1}$)[a]	D_p (nm)[a]	V_p ($cm^3\ g^{-1}$)[a]	BA content ($\mu eq\ g^{-1}$)[b]	LA content ($\mu eq\ g^{-1}$)[c]	Molar ratio of BA/LA[d]
1	*12.2*PW_{12}/ZrO_2-Si(Et)Si-3D_{int}0.5	166	3.3/12.5	0.39	2606.7	2247.1	1.16
2	*12.0*PW_{12}/ZrO_2-Si(Et)Si-3D_{int}/NTs0.75	221	4.7/12.5	0.51	2438.0	2138.6	1.14
3	*12.1*PW_{12}/ZrO_2-Si(Et)Si-NTs1.0	243	4.8/23.1	0.42	2338.3	1981.6	1.18
4	*11.5*PW_{12}/ZrO_2-Si(Et)Si-NTs2.0	519	4.2/23.0	0.99	1188.3	1024.4	1.16
5	*10.4*PW_{12}/ZrO_2-Si(Et)Si-NTs3.0	523	4.2/22.6	0.98	1134.1	746.1	1.52
6	*3.7*PW_{12}/ZrO_2-Si(Et)Si-NTs1.0	311	4.7/30.7	0.64	2231.0	1571.1	1.42
7	*7.0*PW_{12}/ZrO_2-Si(Et)Si-NTs1.0	256	4.8/23.5	0.50	2269.3	1923.1	1.18
8	*14.8*PW_{12}/ZrO_2-Si(Et)Si-NTs1.0	198	4.8/23.1	0.40	2284.7	1903.9	1.20
9	*12.2*PW_{12}/ZrO_2-Si(Et)Si-2D_{hex}1.0	346	4.8	0.46	2363.7	1641.5	1.44
10	*12.1*PW_{12}/ZrO_2-SiO_2-2D_{hex}1.0	364	3.8	0.26	2357.1	1932.0	1.22
11	*12.7*PW_{12}/ZrO_2	138	3.8	0.11	2771.0	1378.6	2.01
12	Amberlyst-15[e]	50	–	–	4800.0	–	–

[a] Surface area (S_{BET}) was calculated using the Brunauer–Emmett–Teller equation; pore diameters (D_p) was calculated using the Barrett–Joyner–Halenda desorption branch of the isotherms; pore volume (V_p) was accumulated up to $P/P_0 = 0.99$.
[b] BA content represents the Brønsted acid-site density, which is determined by acid–base titration.
[c] LA content represents the Lewis acid-site density, which is calculated on the basis of BA content and molar ratio of BA content to LA content.
[d] Molar ratio of BA content to LA content is estimated by the corresponding pyridine FT-IR absorption spectrum.
[e] The data are from Ref. [46].

voltage of 200 kV. Nitrogen porosimetry was performed on a Micromeritics ASAP 2020M surface area and porosity analyzer after the samples were outgassed under vacuum at 363 K for 1 h and 373 K for 4 h. The surface areas were calculated using the Brunauer–Emmett–Teller (BET) equation, while pore size distribution curves were calculated using the Barrett–Joyner–Halenda (BJH) desorption branch of the isotherms, and the pore volume was accumulated up to $P/P_0 = 0.99$. XRD patterns were obtained on a D/max-2200 VPC diffractometer using Cu Kα radiation. Water vapor adsorption isotherms were measured at 298 K with an increase in the pressure using an automated gas sorption analyzer (Quantachrome Autosorb-iQ). The sample was dried under dynamic vacuum at 373 K overnight. Before the measurement, the sample was dried again using the "outgas" function of the surface area analyzer for 12 h at 393 K. For the measurement of water adsorption, a 50 mg sample was used. FT-IR spectra were recorded on a Nicolet Magna 560 IR spectrophotometer. ^{31}P MAS NMR, ^{13}C CP-MAS NMR, and ^{29}Si MAS NMR spectra were recorded on a Bruker AVANCE III 400 WB spectrometer equipped with a 4 mm standard bore CP MAS probe head. The dried and finely powdered samples were packed into a ZrO_2 rotor closed with a Ke-F cap, which was spun at 12 kHz. Chemical shifts for ^{31}P MAS NMR, ^{13}C CP-MAS NMR, and ^{29}Si MAS NMR spectra were referenced to the signal of an $NH_4H_2PO_4$ standard ($\delta = 0.00$), a $C_{10}H_{16}$ standard ($\delta CH_2 = 38.5$), and a 3-(trimethylsilyl)-1-propanesulfonic acid sodium salt standard ($\delta = 0.0$), respectively. The loading of $H_3PW_{12}O_{40}$ in all tested samples is determined using a Leeman Prodigy Spec ICP-AES.

2.4. Determination of the Brønsted acid-site density

The Brønsted acid-site density of as-prepared catalysts was determined by acid–base titration. Fresh catalyst powder (60 mg) was placed in 15 mL deionized water, and the mixture was sealed and stirred at 30 °C for 24 h. The obtained suspension was cooled to room temperature, and then it was titrated with sodium hydroxide solution (4.6 mmol L^{-1}) that had been titrated with a standard potassium hydrogen phthalate solution (5.0 mmol L^{-1}). The Brønsted acid-site density ($\mu eq\ g^{-1}$) could be calculated from the consumed sodium hydroxide [34].

2.5. Pyridine adsorption experiment

The nature of the acid sites (Brønsted and Lewis) of as-prepared catalysts was distinguished by in situ FT-IR spectroscopy with chemical adsorption of pyridine. Catalyst samples were diluted with KBr and pretreated at 100 °C for 12 h under vacuum. The samples were then exposed to pyridine vapor at 60 °C for 12 h under vacuum, followed by pumping out at 150 °C for 1 h to remove the physisorbed pyridine. Then the FT-IR spectra of the catalyst samples adsorbed pyridine were recorded.

The quantification of Lewis and Brønsted acid sites was performed by integrating the area underneath the bands at 1450 and 1540 cm^{-1}, respectively [35], from which the corresponding molar ratio of Brønsted acid-site density to Lewis acid-site density is estimated. On the basis of the molar ratio of Brønsted acid-site density to Lewis acid-site density and of Brønsted acid-site density (determined by titration), Lewis acid-site density is calculated (Table 1).

2.6. Catalytic tests

The catalysts were dried for 2 h at 120 °C under vacuum before the catalytic tests.

2.6.1. Esterification of levulinic acid

Esterification of levulinic acid with various alcohols (e.g., methanol, ethanol, and *n*-butanol) was carried out in a three-necked round-bottomed glass flask fitted with a water-cooled condenser. The reaction was performed under the conditions of alcohol refluxing temperature, atmospheric pressure, 2 wt.% of an air-exposed catalyst, levulinic acid (12.44 mmol) to alcohol (87.08 mmol) molar ratio of 1:7, and constant volume (5 mL). At periodic intervals, 0.1 mL of the reaction mixture was withdrawn and then diluted with acetone to 5 mL. The diluted suspension was centrifuged, and the clear solution was analyzed by a Shimadzu 2014C GC to obtain the concentration of the produced levulinate ester. The GC was coupled with a flame ionization detector and an HP-INNOWAX capillary column (film thickness, 0.5 μm; i.d., 0.32 mm; length, 30 m); the operating temperature was 220 °C and the flow rate of nitrogen gas was 1.0 mL min^{-1}. Ethyl laurate (for methyl levulinate and ethyl levulinate) and methyl levulinate (for *n*-butyl levulinate) were applied as internal standards. The catalytic activity was evaluated quantitatively by the yield of alkyl levulinate (Y, %). Here, $Y\ (\%) = (M_D/M_T) \times 100$, where M_D and M_T is the number of moles of alkyl levulinate produced and expected, respectively.

2.6.2. Ethanolysis of furfuryl alcohol

Ethanolysis of furfuryl alcohol was carried out in an autoclave with a Teflon lining under the conditions of 120 °C, furfuryl alcohol

(1.15 mmol) to ethanol (69.00 mmol) molar ratio of 1:60, and 1.5 wt.% of catalyst; meanwhile, stirring was applied throughout the reaction. The concentrations of the produced ethyl levulinate and 2-(ethoxymethyl)furan were determined periodically on a Shimadzu 2014C gas chromatograph fitted with a HP-INNOWAX capillary column and flame ionization detector. The injection port temperature was 250 °C; the oven temperature was maintained at 60 °C for 5 min and then raised to 180 °C for 10 min at a heating rate of 8 °C min^{-1}. The GC injector temperatures were 250 °C. Ethyl laurate was applied as an internal standard. The catalytic activity of all catalysts was evaluated quantitatively by the yield of ethyl levulinate (Y, %) and turnover frequency (TOF, h^{-1}). TOF (h^{-1}) = $[M_D/(A_{titration} \times m)] \times t^{-1}$, where $A_{titration}$ is the number of equivalents of H^+ determined by acid–base titration, m (g) is the mass of the hybrid catalyst used in ethanolysis reaction, and t (h) is the reaction time. The intermediates produced during the catalytic processes were identified by mass spectrometry coupled with gas chromatography (HP6890GC-5973MSD).

2.6.3. Evaluation of the external mass-transfer limitation

To evaluate the external mass-transfer limitation in current systems, the influence of the stirring rate on the esterification and ethanolysis activity of the PW_{12}/ZrO_2-Si(Et)Si-NTs nanohybrids was studied by selecting *12.1*PW_{12}/ZrO_2-Si(Et)Si-NTs1.0 as the representative catalyst. The catalytic activity of the *12.1*PW_{12}/ZrO_2-Si(Et)Si-NTs1.0 toward both of the target reactions is hardly affected by changing the stirring rate from 400 to 800 or 1200 rpm (Fig. S1 of the electronic Supplementary Information). The result indicated that the PW_{12}/ZrO_2-Si(Et)Si-NTs-catalyzed esterification of levulinic acid and ethanolysis of furfuryl alcohol were free from the external mass-transfer limitation.

3. Results and discussion

3.1. Preparation and characterization of the catalyst

A series of PW_{12}/ZrO_2-Si(Et)Si organic–inorganic hybrid nanocatalysts with various $H_3PW_{12}O_{40}$ loadings (3.7, 7.0, 12.1, and 14.8 wt.%) and initial Si-to-Zr molar ratios (1.0, 2.0, and 3.0) were successfully fabricated by a well-designed P123 single-micelle-templated sol–gel co-condensation route. The procedure includes one-step co-condensation of bridging organosilane (1,2-bis(trimethoxysilyl)ethane) and zirconium *n*-butoxide around triblock copolymer surfactant (P123) micelles in the presence of $H_3PW_{12}O_{40}$. After formation of the Keggin units and ZrO_2 bifunctionalized ethane-bridged organosilica framework, it underwent hydrothermal treatment to further fasten the linkage of the organosilica framework with the Keggin units and ZrO_2. Finally, PW_{12}/ZrO_2-Si(Et)Si was formed after removal of P123 by washing with boiling ethanol (Scheme 1).

Amphiphilic copolymer surfactants (e.g., P123) with both hydrophilic (e.g., PEO) and hydrophobic (e.g., PPO) blocks can readily self-assemble into micelles via hydrogen bonding and hydrophobic/hydrophilic interactions under acidic conditions. The micelles can further aggregate to form lyotropic liquid crystal structures with various morphologies such as rodlike and cylindrical shapes via careful adjustment of preparation conditions. Here, the morphological evolution of the PW_{12}/ZrO_2-Si(Et)Si nanohybrids with 3D interconnected mesostructure, 2D hexagonal periodic mesostructure, and 1D hollow tubular nanostructure is realized by tailoring preparation conditions including the concentration of silica and zirconium precursors (or initial Si-to-Zr molar ratio) and acidity in the initial gel mixture. As illustrated in Scheme 1 and displayed in Fig. 1a, at a P123-to-Si-to-Zr-to-HCl molar ratio of 0.0168:0.5:1:6, the PW_{12}/ZrO_2-Si(Et)Si nanohybrid mainly displays a disordered 3D interconnected mesostructure, accompanied by a few 1D hollow tubular particles. As increasing initial Si-to-Zr molar ratio to 0.75 and at P123-to-Si-to-Zr-to-HCl molar ratio of 0.0168:0.75:1:6, the PW_{12}/ZrO_2-Si(Et)Si nanohybrid exhibits both a disordered 3D interconnected mesostructure and a 1D hollow tubular nanostructure (Fig. 1b). When the initial Si-to-Zr molar ratio is continuously increased to 1.0, 2.0, and 3.0, the PW_{12}/ZrO_2-Si(Et)Si nanohybrid mainly exhibits a 1D hollow tubular nanostructure, and the estimated inner diameter, shell thickness, and particle size of the tubes are 4–5, 3, and 10–11 nm, respectively (Fig. 1c–e). At the same amount of added P123 and initial Si-to-Zr molar ratio of 1.0 but a significant decrease in the acidity, e.g., at a P123-to-Si-to-Zr-to-HCl molar ratio of 0.0168:1:1:2, the morphology of the PW_{12}/ZrO_2-Si(Et)Si nanohybrid is transformed to a 2D hexagonal periodic mesostructure (Fig. 1f). A similar morphology can also be found in the PW_{12}/ZrO_2-SiO_2 nanohybrid prepared at a P123-to-Si-to-Zr-to-HCl molar ratio of 0.0168:1:1:6 using TEOS rather than BTMSE as the Si source (Fig. 1g). In this case, fabrication of 2D hexagonal ordered mesoporous PW_{12}/ZrO_2-SiO_2 is realized at higher rather than lower acidity. This is due to the fact that the organosilane precursor with bridging ethyl groups has quite different properties from TEOS, for example, the hydrolysis and condensation rate, the hydro phobicity/hydrophilicity, and the rigidity [10]. However, in the absence of a silicon precursor, neither tubular nor ordered nanostructure can be formed (i.e., *12.7*PW_{12}/ZrO_2, Fig. 1h), implying the important morphology-adjusting function of the silicon precursor.

On the basis of these results, it is inferred that at a suitable concentration of P123 micelles, the Si-to-Zr molar ratio and acidity in the initial gel mixture play the key roles in fabrication of PW_{12}/ZrO_2-Si(Et)Si nanohybrids with different morphologies. The influence of the initial Si-to-Zr molar ratio on the morphological evolution of the PW_{12}/ZrO_2-Si(Et)Si nanohybrids is explained in terms of the hydrolysis/condensation rate and hydrophobicity/hydrophilicity of the precursors (e.g., BTMSE and $Zr(OC_4H_9)_4$) [10]. On one hand, P123 is capable of self-assembly into single rodlike micelles in strong acidic media. The $Zr(OC_4H_9)_4$ precursor with a faster hydrolysis/condensation rate can produce more hydrolyzed species (e.g., $Zr(OC_4H_9)_{4-x}(OH_2^+)_x$) to condense around P123 single rodlike micelles, which in turn results in the aggregation of single rodlike micelles and the formation of 3D interconnected mesostructure. However, the hydrolysis/condensation rate of BTMSE is much slower than that of $Zr(OC_4H_9)_4$, and increasing the initial Si-to-Zr molar ratio (e.g., 1.0, 2.0, or 3.0) can slow the hydrolysis/condensation rate of the precursors, which effectively inhibits the aggregation of P123 single rodlike micelles and readily forms a 1D hollow tubular nanostructure. On the other hand, the morphology of the hybrid materials is related to the hydrophobicity/hydrophilicity of the precursors. BTMSE with bridging ethyl groups is a hydrophobic precursor compared with $Zr(OC_4H_9)_4$. Formation of P123 single rodlike micelles can be encouraged by the hydrophobic unhydrolyzed BTMSE, since the charge density on the surface of P123 micelles is decreased owing to the penetration of the hydrophobic unhydrolyzed BTMSE into the micelles. With increasing initial Si-to-Zr molar ratio, the enhanced hydrophobicity in the preparation system leads to the formation of a 1D hollow tubular morphology. Therefore, it is concluded that changing initial Si-to-Zr molar ratios in the preparation systems can adjust the hydrolysis/condensation rate and hydrophobicity/hydrophilicity of the precursors, which in turn leads to PW_{12}/ZrO_2-Si(Et)Si nanohybrids with a 3D interconnected mesostructure or a 1D hollow tubular nanostructure.

Additionally, at the same added amount of P123 and initial Si-to-Zr molar ratio but a significantly decreased concentration of HCl, e.g., a P123-to-Si-to-Zr-to-HCl molar ratio of 0.0168:1:1:2, the morphology of PW_{12}/ZrO_2-Si(Et)Si transforms to a 2D hexagonal periodic mesostructure. The result suggests that the acidity of the preparation system also plays an important role in the

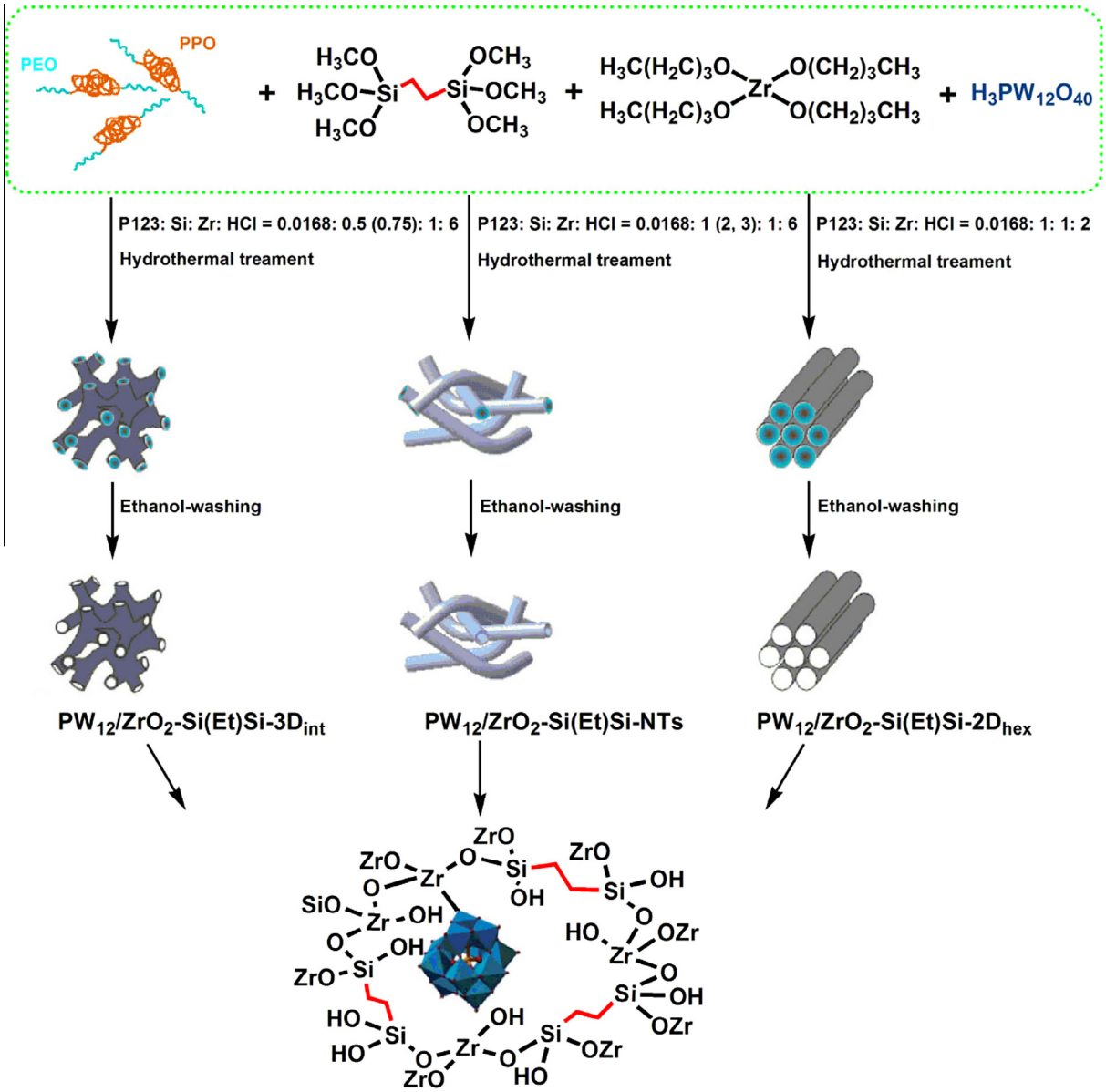

Scheme 1. Illustration of P123-templated one-step preparation of the PW_{12}/ZrO_2-Si(Et)Si nanohybrids with 1D hollow tubular nanostructure, 2D hexagonal periodic mesostructure and 3D interconnected mesostructure as well as its wall composition.

construction of PW_{12}/ZrO_2-Si(Et)Si nanohybrids with different morphologies. At higher acidity (e.g., P123-to-Si-to-Zr-to-HCl molar ratio 0.0168:1:1:6), single rodlike P123 lyotropic liquid crystal phases are formed by self-assembly, in which hydrophobic PPO blocks form a core of the micelles, while hydrophilic PEO blocks form a hydrated corona around the core; meanwhile, higher acidity can facilitate co-hydrolysis and -condensation of BTMSE and Zr $(OC_4H_9)_4$ at a higher rate, which is favorable to the formation of individual hollow tubular nanohybrids. In contrast, at lower acidity, e.g., P123-to-Si-to-Zr-to-HCl molar ratio 0.0168:1:1:2, P123 micelles can aggregate linearly to form a 2D hexagonal lyotropic liquid crystal structure; meanwhile, lower acidity can lower the co-hydrolysis and -condensation rates of BTMSE and $Zr(OC_4H_9)_4$, which is favorable to formation of nanohybrids with a 2D hexagonal periodic mesostructure instead of an individual hollow tubular nanostructure.

3.1.1. Textural properties

Nitrogen gas porosimetry measurements can support the above TEM observations. From Fig. 2a, c, and e it is found that all tested samples exhibit a type IV isotherm, indicating their mesoporosity. Interestingly, the PW_{12}/ZrO_2-Si(Et)Si hybrid nanocatalysts with different morphologies possess different hysteresis loop shapes (Fig. 2a and e), reflecting the influence of morphology on the porosity properties. *12.2*PW_{12}/ZrO_2-Si(Et)Si-3D$_{int}$0.5 and *12.0*PW_{12}/ZrO_2-Si(Et)Si-3D$_{int}$/NTs0.75 exhibit an H2 hysteresis loop that appears at higher relative pressure (P/P_0), e.g., 0.75–0.99, implying they both possess disordered a 3D interconnected mesostructure with larger pore size. From Fig. 2a it is also found that three tubular PW_{12}/ZrO_2-Si(Et)Si nanocatalysts all exhibit two capillary condensation steps at P/P_0 = 0.45–0.70 and 0.80–0.99. Combining the textural properties with the morphological characteristics of the tubular PW_{12}/ZrO_2-Si(Et)Si nanocatalysts, it is speculated that the

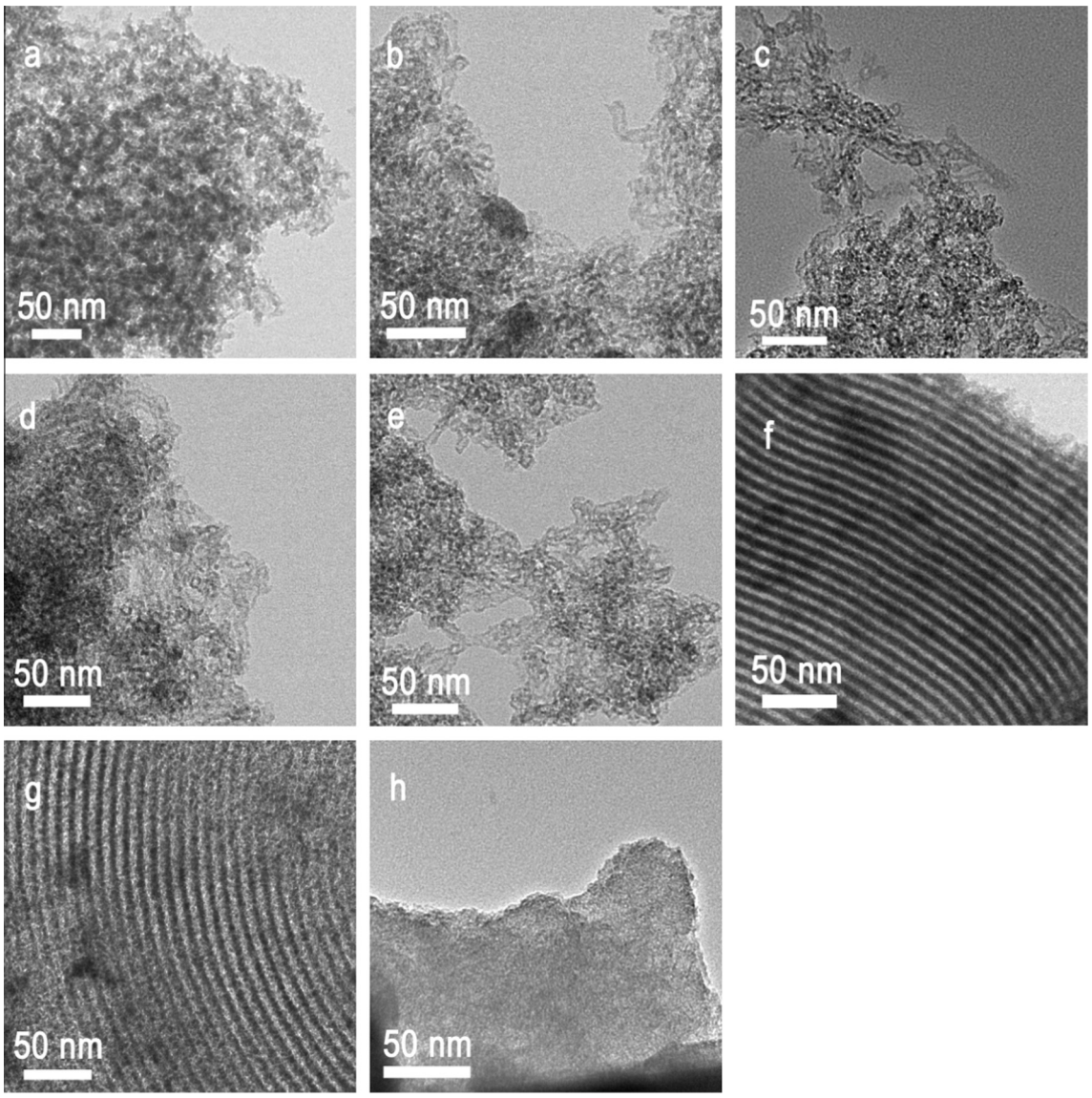

Fig. 1. TEM images of (a) *12.2*PW_{12}/ZrO_2-Si(Et)Si-3D_{int}0.5, (b) *12.0*PW_{12}/ZrO_2-Si(Et)Si-3D_{int}/NTs0.75, (c) *12.1*PW_{12}/ZrO_2-Si(Et)Si-NTs1.0, (d) *11.5*PW_{12}/ZrO_2-Si(Et)Si-NTs2.0, (e) *10.4*PW_{12}/ZrO_2-Si(Et)Si-NTs3.0, (f) *12.2*PW_{12}/ZrO_2-Si(Et)Si-2D_{hex}1.0, (g) *12.1*PW_{12}/ZrO_2-SiO_2-2D_{hex}1.0, and (h) *12.7*PW_{12}/ZrO_2.

first capillary condensation step at lower P/P_0 is due to the hollow interior of the nanotube channel, and that the other capillary condensation step at higher relative pressure originates from the void space between the loosely packed tubular particles. Similar results have been separately reported by Yang's, Kruk's, and our groups [10,17,36]. Therefore, the tubular PW_{12}/ZrO_2-Si(Et)Si nanohybrids possess a bimodal pore structure. These results are in line with the BJH pore-size distribution curves displayed in Fig. 2b as well as the textural parameters summarized in Table 1. For the PW_{12}/ZrO_2-Si(Et)Si nanocatalysts prepared at various initial Si-to-Zr molar ratios (e.g., 0.5, 0.75, 1.0, 2.0, and 3.0) and similar $H_3PW_{12}O_{40}$ loading (10.4–12.2 wt.%), the primary and secondary pore diameters calculated from BJH adsorption determination are in the range of 3.3–4.7 and 12.5–23.0 nm, respectively; additionally, their BET surface area (166–523 $m^2\,g^{-1}$) and pore volume (0.39–0.99 $cm^3\,g^{-1}$) increase gradually (entries 1–5 of Table 1). Therefore, it is inferred that the textural properties of the PW_{12}/ZrO_2-Si(Et)Si nanohybrids can be significantly improved by the introduction of a suitable amount of bridged silsesquioxane into the preparation system.

Fig. 2c and d presents the nitrogen gas sorption isotherms and BJH pore-size distribution curves of the PW_{12}/ZrO_2-Si(Et)Si-NTs1.0 nanocatalysts with various $H_3PW_{12}O_{40}$ loadings, showing little influence of $H_3PW_{12}O_{40}$ loading on the type of the isotherms and shape of the pore-size distribution curves. Through analyzing the textural parameters summarized in Table 1, it is found that the BET surface area (311–198 $m^2\,g^{-1}$) and pore volume (0.64–0.40 $cm^3\,g^{-1}$) of the four tested samples decrease gradually as $H_3PW_{12}O_{40}$ loading increases from 3.7 to 14.8 wt.% (entries 3, 6–8 of Table 1). The result implies that most of the Keggin units are confined inside the tubes, since 1D tubular PW_{12}/ZrO_2-Si(Et)Si nanohybrids possess a large fraction of voids in the interior. Therefore, incorporation of a large amount of the Keggin units could block the channel of the tubes severely, which in turn leads to the decreased BET surface area and pore volume.

As for the *12.2*PW_{12}/ZrO_2-Si(Et)Si-2D_{hex}1.0 and *12.1*PW_{12}/ZrO_2-SiO_2-2D_{hex}1.0 nanohybrids, they both exhibit a type IV isotherm with an H1 hysteresis loop, indicating their periodic or ordered mesostructure (Fig. 2e). The sharp BJH pore-size distribution curves also indicate a uniform pore size of the nanohybrids

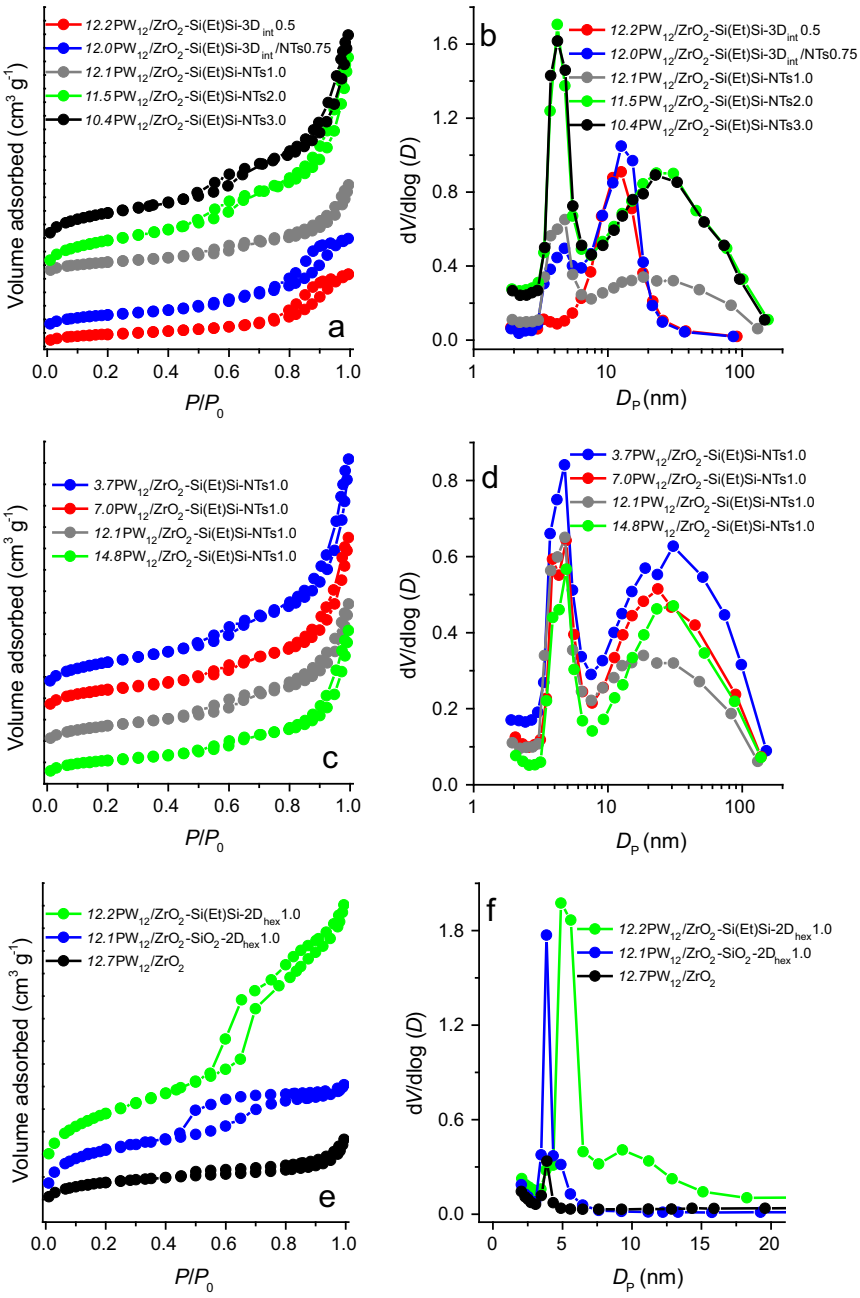

Fig. 2. Nitrogen gas adsorption/desorption isotherms and pore size distribution curves of various PW_{12}/ZrO_2-based nanohybrids.

(Fig. 2f); additionally, the capillary condensation step occurs at lower and higher P/P_0 for the *12.1*PW_{12}/ZrO_2-SiO_2-2D_{hex}1.0 (0.40–0.99) and *12.2*PW_{12}/ZrO_2-Si(Et)Si-2D_{hex}1.0 (0.50–0.99), suggesting their smaller (3.8 nm) and larger (4.8 nm) pore diameters (Table 1). However, the *12.1*PW_{12}/ZrO_2-SiO_2-2D_{hex}1.0 and *12.2*PW_{12}/ZrO_2-Si(Et)Si-2D_{hex}1.0 possess similar BET surface area (364 and 346 $m^2\ g^{-1}$, entries 9 and 10 of Table 1). Low-angle XRD measurement is applied to further verify the periodic or ordered mesostructure of the *12.2*PW_{12}/ZrO_2-Si(Et)Si-2D_{hex}1.0 and *12.1*PW_{12}/ZrO_2-SiO_2-2D_{hex}1.0 nanohybrids. From the result displayed in Fig. S2 of the electronic Supplementary Information it is found that the nanohybrids exhibit diffraction peaks at 0.84° and 0.76°, respectively, which is indexed as the (100) Bragg reflection of the 2D hexagonal *p6mm* mesostructure. However, two weak Bragg reflections of (110) and (200) (in the range of 1.0°–2.0°) fail to be detected. The result may be due to the fact that the existence of ZrO_2 in the nanohybrids may interfere with the observation of both of the weak peaks. A similar result has also been found in our previously prepared ordered PW_{12}/ZrO_2-Si(Et/Ph)Si materials [30]. Nevertheless, the long-range structural ordering of the *12.2*PW_{12}/ZrO_2-Si(Et)Si-2D_{hex}1.0 and *12.1*PW_{12}/ZrO_2-SiO_2-2D_{hex}1.0 nanohybrids can be clearly observed by TEM (Fig. 1f and g) and nitrogen gas porosimetry measurements (Fig. 2e and f).

In the case of *12.7*PW_{12}/ZrO_2, the shape of the hysteresis loop is irregular, together with its having the lowest nitrogen gas adsorbed amount (Fig. 2e). By combining the BJH pore-size distribution curves presented in Fig. 2f with the textural parameters summarized in Table 1, it is found that the mesoporosity of the *12.7*PW_{12}/ZrO_2 material is poor. Compared with the *12.1*PW_{12}/ZrO_2-Si(Et)Si-NTs1.0 material, the *12.7*PW_{12}/ZrO_2 possesses smaller BET surface area (138 $m^2\ g^{-1}$) and pore diameter (3.8 nm) as well as lower pore volume (0.11 $cm^3\ g^{-1}$, entry 11 of Table 1).

This result further indicates that incorporation of ethane-bridged organosilica units into the framework of the nanocatalysts can improve their morphological characteristics and textural properties.

Additionally, to compare the hydrophilicity/hydrophobicity of as-prepared PW_{12}/ZrO_2-Si(Et)Si-NTs nanohybrids with that of alkyl-free PW_{12}/ZrO_2-SiO_2, water vapor adsorption measurement is carried out at 298 K with an increase in the pressure using an automated gas sorption analyzer, and *12.1*PW_{12}/ZrO_2-Si(Et)Si-NTs1.0, *10.4*PW_{12}/ZrO_2-Si(Et)Si-NTs3.0 and *12.1*PW_{12}/ZrO_2-SiO_2-$2D_{hex}$1.0 are selected as the representatives. Based on the literature work [37] and the determined water vapor adsorption isotherms (Fig. S3 of the electronic Supplementary Information) as well as nitrogen gas adsorption isotherms (Fig. 2a and e), the degree of the surface hydrophobicity of the tested nanohybrids is estimated by the ratio of water vapor uptake volume (V_{H2O}) to nitrogen uptake volume (V_{N2}) measured at relative pressure $P/P_0 = 0.15$. This value, which is denoted as $x_{0.15}$, serves as a good standard to evaluate the surface hydrophobicity of the tested nanohybrids by considering factors including the ability to adsorb water molecules and the porosity properties of the nanohybrids simultaneously. A lower $x_{0.15}$ value indicates that the surface of the nanohybrids is more hydrophobic. Herein, the calculated $x_{0.15}$ values of *10.4*PW_{12}/ZrO_2-Si(Et)Si-NTs3.0, *12.1*PW_{12}/ZrO_2-Si(Et)Si-NTs1.0, and *12.1*PW_{12}/ZrO_2-SiO_2-$2D_{hex}$1.0 are 0.37, 0.79, and 0.89, respectively. The result suggests that the incorporation of ethane-bridged organosilica units into the framework of the nanohybrids indeed improves the surface hydrophobicity; meanwhile, greater content of ethane-bridged organosilica units in the framework can create stronger surface hydrophobicity.

3.1.2. Composition and structural information

The structural integrity of the Keggin units and the formation of a carbon/silica framework, as well as the interaction between ZrO_2 and organic or inorganic functionalities in the hollow tubular organic–inorganic hybrid nanocatalysts, are confirmed by FT-IR (Fig. 3a), ^{31}P MAS NMR (Fig. 4a and b), ^{13}C CP-MAS NMR (Fig. 4c), and ^{29}Si MAS NMR (Fig. 4d) spectra.

FT-IR spectra displayed in Fig. 3a indicates that the parent $H_3PW_{12}O_{40}$ shows four characteristic vibrational peaks at 1080, 983, 893, and 795 cm^{-1}, respectively, which are assigned to the stretching vibrations of tetrahedral P—O bonds, terminal W=O bonds, and two types of bridging W—O—W bonds of the Keggin clusters [38]. After formation of the *12.7*PW_{12}/ZrO_2 hybrid material, the above characteristic vibrational peaks still can be found at 1080, 982, 896, and 820 cm^{-1}, implying that the primary Keggin structure remains intact after the immobilization. A shift of the vibration frequency of the W—O—W bond implies strong interaction between the Keggin units and the ZrO_2 support, which can be confirmed by following ^{31}P MAS NMR (Fig. 4b). After the introduction of ethane-bridged organosilica units into the PW_{12}/ZrO_2 framework, the four characteristic vibrational peaks related to the parent Keggin units still can be found; however, their peak intensities decrease. Interestingly, compared with the parent $H_3PW_{12}O_{40}$ or *12.7*PW_{12}/ZrO_2 material, a new weak peak is found at 1030 cm^{-1} for the PW_{12}/ZrO_2-Si(Et)Si hybrid materials, regardless of their morphologies. This peak is assigned to the stretching vibrations of the Zr—O—Si bond [39], providing direct evidence that ethane-bridged organosilica groups are incorporated into the ZrO_2 framework via Zr—O—Si—C—Si covalent linkages. Additionally, the peaks appeared at 2975 and 2895 cm^{-1} are assigned to the asymmetric and symmetric stretching vibrations of the C—H bond of the —Si—CH_2—CH_2—Si— units, further confirming that ethane-bridged organosilica units are as bridging component directly introduced into ZrO_2 framework through —Zr—O—Si—C—C—Si—O— linkages.

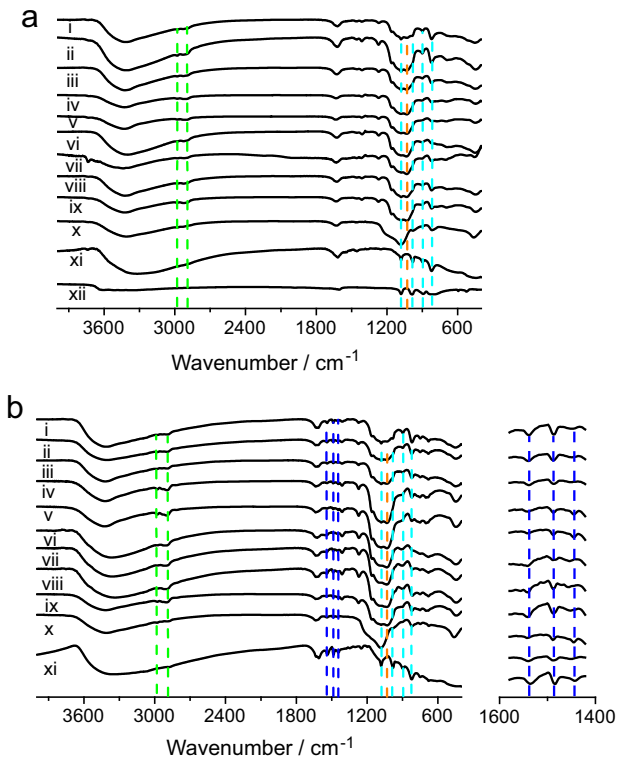

Fig. 3. FT-IR spectra (a) and pyridine-adsorbed FT-IR spectra (b) of *12.2*PW_{12}/ZrO_2-Si(Et)Si-$3D_{int}$0.5 (i), *12.0*PW_{12}/ZrO_2-Si(Et)Si-$3D_{int}$/NTs0.75 (ii), *12.1*PW_{12}/ZrO_2-Si(Et)Si-NTs1.0 (iii), *11.5*PW_{12}/ZrO_2-Si(Et)Si-NTs2.0 (iv), *10.4*PW_{12}/ZrO_2-Si(Et)Si-NTs3.0 (v), *3.7*PW_{12}/ZrO_2-Si(Et)Si-NTs1.0 (vi), *7.0*PW_{12}/ZrO_2-Si(Et)Si-NTs1.0 (vii), *14.8*PW_{12}/ZrO_2-Si(Et)Si-NTs1.0 (viii), *12.2*PW_{12}/ZrO_2-Si(Et)Si-$2D_{hex}$1.0 (ix), *12.1*PW_{12}/ZrO_2-SiO_2-$2D_{hex}$1.0 (x), and *12.7*PW_{12}/ZrO_2 (xi). The comparative spectrum of $H_3PW_{12}O_{40}$ (xii) is also shown.

It should be admitted that the stretching vibrations of Si—O bonds from the ethane-bridged organosilica fragments also appear at ca. 1080 cm^{-1}, which may interfere with the observation of the vibrations of tetrahedral P—O bonds within the Keggin units [40]. Therefore, the structural integrity of the Keggin units in the *12.1*PW_{12}/ZrO_2-Si(Et)Si-NTs1.0 nanohybrid is further confirmed by ^{31}P MAS NMR, and the starting $H_3PW_{12}O_{40}$ is also tested as the reference. The starting $H_3PW_{12}O_{40}$ only exhibits one strong resonance signal at −16.5 ppm (Fig. 4a), originating from the resonance of PO_4 units within the bulk $H_3PW_{12}O_{40}$ environment. In the case of the *12.1*PW_{12}/ZrO_2-Si(Et)Si-NTs1.0 nanohybrid, two peaks are detected (Fig. 4b): the intense signal at −16.5 ppm is assigned to the resonance of PO_4 units of the starting $H_3PW_{12}O_{40}$, while the weak signal at −11.5 ppm is assigned to $(\equiv ZrOH_2)_n{}^+[H_{3-n}PW_{12}O_{40}]^{n-}$ species formed at the interface between the Keggin units and the ZrO_2 support [30]. The result provides powerful evidence to confirm the structural integrity of the Keggin units after the heterogenization; moreover, the Keggin units link the ZrO_2 support via Zr—O—W covalent bonds at the interface of two components.

The formation of a carbon/silica framework in the *12.1*PW_{12}/ZrO_2-Si(Et)Si-NTs1.0 nanohybrid is further confirmed by ^{13}C CP-MAS NMR and ^{29}Si MAS NMR spectra. In the ^{13}C CP-MAS NMR spectrum of the *12.1*PW_{12}/ZrO_2-Si(Et)Si-NTs1.0 (Fig. 4c), the predominant peak at 5.2 ppm originates from the carbon species of bridging ethyl groups in organosilica units (—Si—CH_2—CH_2—Si—) [41], suggesting that ethane-bridged organosilica units are successfully incorporated into the framework of the nanohybrids through —Zr—O—Si—CH_2—CH_2—Si—O— linkages. In the cases of four weak signals at 70.2, 57.7, 16.8, and

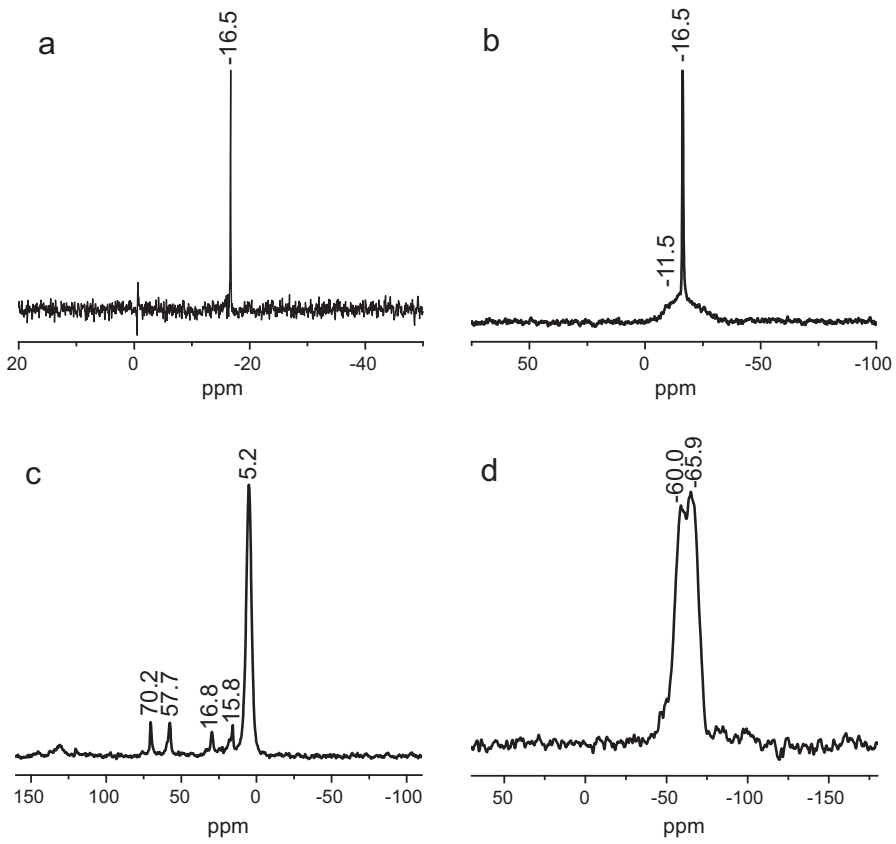

Fig. 4. ^{31}P MAS NMR spectra of the starting $H_3PW_{12}O_{40}$ (a) and the *12.1*PW_{12}/ZrO_2-Si(Et)Si-NTs1.0 nanohybrid (b); ^{13}C CP-MAS NMR (c) and ^{29}Si MAS NMR (d) spectra of the *12.1*PW_{12}/ZrO_2-Si(Et)Si-NTs1.0 nanohybrid.

15.8 ppm, they are assigned to residual P123 and the carbon species of the ethoxy group that are formed during the boiling ethanol washing process [42,43]. In the ^{29}Si MAS NMR spectrum of the *12.1*PW_{12}/ZrO_2-Si(Et)Si-NTs1.0 (Fig. 4d), two characteristic resonances at −60.0 and −65.9 ppm correspond to the organosiloxane species such as —CH_2CH_2—Si$(OSi)_2(OH)$ (T^2) and —CH_2CH_2—Si$(OSi)_3$ (T^3) within the carbon/silica framework of the nanohybrids, respectively; meanwhile, the absence of any resonance signal corresponding to inorganic SiO_4 species such as Q^3[$Si(OSi)_3(OH)$, −90 ppm] and Q^4[$Si(OSi)_4$, −120 ppm] confirms that cleavage of the Si—C bond in the silica/carbon framework of the *12.1*PW_{12}/ZrO_2-Si(Et)Si-NTs1.0 can be avoided.

Based on the above structural information, the wall composition of the PW_{12}/ZrO_2-Si(Et)Si-NTs nanohybrids is proposed and illustrated in Scheme 1.

3.1.3. Brønsted and Lewis acidity

The PW_{12}/ZrO_2-Si(Et)Si hybrid nanocatalysts possess both Brønsted and Lewis acidity, contributed by both $H_3PW_{12}O_{40}$ and ZrO_2 [25,26]; meanwhile, the Brønsted acidity of the Keggin units and ZrO_2 is further enhanced due to strong W—O—Zr covalent binding between $H_3PW_{12}O_{40}$ clusters and ZrO_2 support, which can promote the release of the protons [19,27–30].

In situ pyridine FT-IR determination is applied to characterize the nature of the acid sites in as-prepared PW_{12}/ZrO_2-Si(Et)Si hybrid nanocatalysts. Compared with FT-IR spectra of pyridine-free *12.1*PW_{12}/ZrO_2-Si(Et)Si-NTs1.0 sample (Fig. 3a), FT-IR spectra of pyridine adsorbed on the PW_{12}/ZrO_2-Si(Et)Si samples show three new peaks positioned at 1450, 1490, and 1540 cm^{-1} (Fig. 3b). The peak at 1450 cm^{-1} is assigned to the Lewis acid sites, which are due to pyridine coordinatively bonding to the unsaturated surface Zr^{4+} sites of ZrO_2 [44]. As for the peak at 1540 cm^{-1}, it is related to pyridinium ions formed due to protonation of the Brønsted acid sites [25]. These Brønsted acid sites are contributed from the protons of $H_3PW_{12}O_{40}$ and surface Zr—OH groups of ZrO_2. The co-existence of Brønsted and Lewis acid sites is confirmed by the characteristic peak at 1490 cm^{-1}.

Subsequently, the Brønsted acid-site density of the PW_{12}/ZrO_2-Si(Et)Si hybrid materials is measured through acid–base titration with dilute NaOH. As shown in Table 1, at a similar $H_3PW_{12}O_{40}$ loading (10.4–12 wt.%) but different initial Si-to-Zr molar ratios, the Brønsted acid-site density of the PW_{12}/ZrO_2-Si(Et)Si nanohybrids (2607, 2438, and 2338 μeq g^{-1}) decreases gradually with increasing Si-to-Zr molar ratios from 0.5 to 0.75 and 1.0, and with further increasing initial Si-to-Zr molar ratio to 2.0 or 3.0, the acid-site density of the PW_{12}/ZrO_2-Si(Et)Si (1188 and 1134 μeq g^{-1}) decreases significantly (entries 1–5 of Table 1). This is due to the fact that the proportion of nonacidic silica in the nanohybrids increases and goes parallel with the initial Si-to-Zr molar ratio from 0.5 to 3.0. As for the four tubular PW_{12}/ZrO_2-Si(Et)Si-NTs nanohybrids prepared at an initial Si-to-Zr molar ratio of 1.0 but different $H_3PW_{12}O_{40}$ loadings, the Brønsted acid-site density increases gradually from 2231 to 2338 μeq g^{-1} with increasing $H_3PW_{12}O_{40}$ loading from 3.7 to 12.1 wt.% (entries 3, 6, and 7 of Table 1). Nevertheless, when $H_3PW_{12}O_{40}$ loading increases further to 14.8 wt.%, the acid-site density of the PW_{12}/ZrO_2-Si(Et)Si-NTs-1.0 decreases slightly (2285 μeq g^{-1}, entry 8 of Table 1). The result may be due to the agglomeration of some $H_3PW_{12}O_{40}$ clusters. Additionally, at the same initial Si-to-Zr molar ratio (1.0) and $H_3PW_{12}O_{40}$ loading (ca. 12 wt.%), the periodic mesostructured PW_{12}/ZrO_2-Si(Et)Si-2D_{hex} nanohybrids, i.e., *12.2*PW_{12}/ZrO_2-Si(Et)Si-2D_{hex}1.0 and *12.1*PW_{12}/ZrO_2-SiO_2-2D_{hex}1.0, possess similar acid-site densities (2364 and

2357 μeq g^{-1}, entries 9 and 10 of Table 1) to their hollow tubular counterpart (*12.1*PW_{12}/ZrO_2-Si(Et)Si-NTs1.0). In the case of the *12.7*PW_{12}/ZrO_2, its acid-site density (2771 μeq g^{-1}, entry 11 of Table 1) is the highest among all tested PW_{12}/ZrO_2-based nanohybrids, since no silica component is included in it.

Finally, the Lewis acid-site density of the PW_{12}/ZrO_2-Si(Et)Si nanohybrids is calculated on the basis of the molar ratio of Brønsted acid-site density (BA) to Lewis acid-site density (LA) as well as of the Brønsted acid-site density (Table 1). Here, the molar ratio of BA/LA is estimated by the corresponding pyridine FT-IR absorption spectrum, and the quantification of Lewis and Brønsted acid sites has been performed by integrating the area underneath the bands at 1450 and 1540 cm^{-1}, respectively [35]. The Lewis acid-site density generally decreases as Si-to-Zr molar ratios increase from 0.5, 0.75, 1.0, and 2.0 to 3.0 (entries 1–5 of Table 1).

3.2. Heterogeneous acid catalytic performance

3.2.1. Esterification of levulinic acid

The heterogeneous acid catalytic activity of PW_{12}/ZrO_2-Si(Et)Si hybrid nanocatalysts with various morphologies is evaluated by esterification of levulinic acid with methanol to yield methyl levulinate at a levulinic acid-to-methanol molar ratio of 1:7 (which can drive the equilibrium to the ester product), 2 wt.% catalyst, 65 °C, and atmospheric pressure (Scheme 2).

First, the catalytic activity of the PW_{12}/ZrO_2-Si(Et)Si hybrid nanocatalysts prepared with various initial Si-to-Zr molar ratios (0.5, 0.75, 1.0, 2.0, and 3.0) is compared, and the results are shown in Fig. 5. At similar $H_3PW_{12}O_{40}$ loading (10.4–12.2 wt.%) and lower initial Si-to-Zr molar ratios (0.5, 0.75, and 1.0), the esterification activity of the PW_{12}/ZrO_2-Si(Et)Si nanohybrids increases with initial Si-to-Zr molar ratios; for example, after the reaction is carried out for 60 min, the yield of methyl levulinate reaches 82.9, 83.2, and 99.9%, respectively, for the *12.2*PW_{12}/ZrO_2-Si(Et)Si-$3D_{int}$0.5-, *12.0*PW_{12}/ZrO_2-Si(Et)Si-$3D_{int}$/NTs0.75-, and *12.1*PW_{12}/ZrO_2-Si(Et)Si-NTs1.0-catalyzed esterification reactions. However, for the PW_{12}/ZrO_2-Si(Et)Si nanohybrids obtained at higher initial Si-to-Zr molar ratios (2.0 and 3.0), the esterification activity is lower. That is, for the *11.5*PW_{12}/ZrO_2-Si(Et)Si-NTs2.0- and *10.4*PW_{12}/ZrO_2-Si(Et)Si-NTs3.0-catalyzed esterification reactions, the yield of methyl levulinate reaches 67.1 and 60.4%, respectively, over a period of 60 min. This result suggests that both the morphological characteristics and the Brønsted acid site density of the PW_{12}/ZrO_2-Si(Et)Si hybrid nanocatalysts play dominant roles in the esterification activity. With the initial Si-to-Zr molar ratio increased from 0.5 to 0.75 and 1.0, the morphological evolution of the PW_{12}/ZrO_2-Si(Et)Si nanohybrids with 3D interconnected mesostructure, mixed 3D interconnected mesostructure, and 1D hollow tubular nanostructure to a perfect 1D hollow tubular nanostructure takes place. The disordered mesostructure can increase the diffusion and mass transfer resistance, leading to poor accessibility of the acid sites to the reactants. Otherwise, 1D hollow tubular PW_{12}/ZrO_2-Si(Et)Si nanohybrids possess a large fraction of voids in the interior, allowing most of the Keggin units to be confined inside the tubes. The acid-site-confined hollow interiors of the tubular nanohybrids can provide nanoreactors for esterification reactions, ensuring efficient reactant diffusion and acid site accessibility during the reaction. Additionally, the extremely thin wall of *12.1*PW_{12}/ZrO_2-Si(Et)Si-NTs1.0 can significantly facilitate mass transfer of the reactant/product through successful reduction of the mass transfer resistance from the nanotubes' outside surface to the interior. Therefore, *12.1*PW_{12}/ZrO_2-Si(Et)Si-NTs1.0 is the most active among the three PW_{12}/ZrO_2-Si(Et)Si nanohybrids obtained at initial Si-to-Zr molar ratios of 0.5, 0.75, and 1.0, although its Brønsted acid site density (2338 μeq g^{-1}) is lower than that of *12.2*PW_{12}/ZrO_2-Si(Et)Si-$3D_{int}$0.5 (2607 μeq g^{-1}) or *12.0*PW_{12}/ZrO_2-Si(Et)Si-$3D_{int}$/NTs0.75 (2438 μeq g^{-1}). However, for the PW_{12}/ZrO_2-Si(Et)Si nanohybrids prepared at initial Si-to-Zr molar ratios of 2.0 and 3.0, although they still possess a 1D hollow tubular nanostructure and excellent textural properties including a much greater BET surface area (519 and

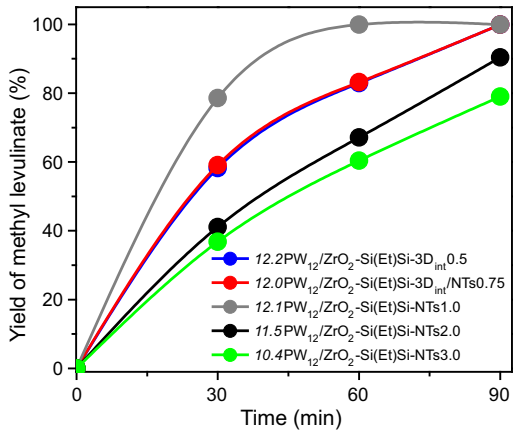

Fig. 5. Catalytic activity comparison of various PW_{12}/ZrO_2-Si(Et)Si nanohybrids in esterification of levulinic acid (12.44 mmol) with methanol (87.08 mmol) to yield methyl levulinate: 2 wt.% catalyst, 65 °C, atmospheric pressure.

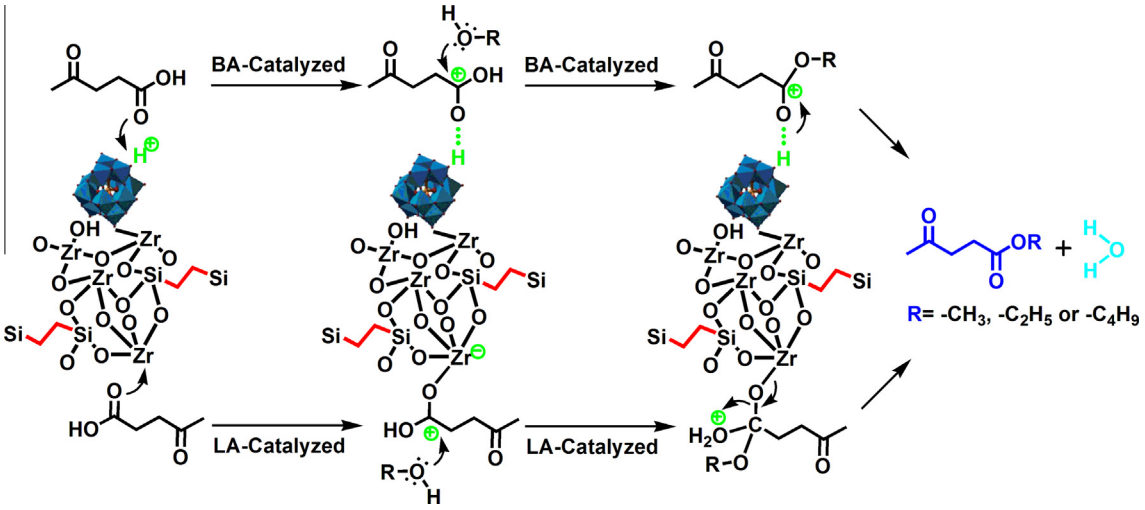

Scheme 2. Possible reaction mechanism of synthesis of alkyl levulinates from esterification of levulinic acid catalyzed over the PW_{12}/ZrO_2-Si(Et)Si-NTs nanohybrids.

523 $m^2 g^{-1}$) as well as a higher pore volume (0.99 and 0.98 $cm^3 g^{-1}$), their obviously decreased Brønsted acid site density (1188 and 1134 μeq g^{-1}) compared with that of *12.1*PW_{12}/ZrO_2-Si(Et)Si-NTs1.0 results in lower esterification activity. Therefore, it is inferred that the Brønsted acid site density of the PW_{12}/ZrO_2-Si(Et)Si hybrid nanocatalyst plays the paramount role in its esterification activity, and higher Brønsted acid site densities can facilitate the reaction proceeding at a faster rate.

Additionally, it should be noted that the increased surface hydrophobicity owing to the introduction of ethane-bridged organosilica units into the PW_{12}/ZrO_2 framework is also helpful in improving the acid catalytic activity of the hybrid nanocatalysts. PW_{12}/ZrO_2 itself is hydrophilic due to the existence of surface ≡Zr—OH groups. For the PW_{12}/ZrO_2-catalyzed esterification reaction, the yielded water molecules are favored to adsorb on the surface of the hydrophilic PW_{12}/ZrO_2. Moreover, esterification is a reversible process, and the produced ester molecules can easily be hydrolyzed by water, so that the reaction is suppressed to some extent. These problems can be moderated by functionalization of PW_{12}/ZrO_2 with hydrophobic ethane-bridged organosilica units, which can selectively create an unsuitable environment for water molecules and cause them to escape from the catalyst surface easily. Consequently, the accessibility of the acid sites to levulinic acid may be increased; meanwhile, deactivation of the acid sites owing to the strong adsorption of water molecules on the catalyst surface is inhibited, which is confirmed by the following recycling tests.

Subsequently, the influence of $H_3PW_{12}O_{40}$ loading on the catalytic activity of tubular PW_{12}/ZrO_2-Si(Et)Si nanohybrids is studied. From the results shown in Fig. 6 it is found that the tested catalysts follow the activity order *12.1*PW_{12}/ZrO_2-Si(Et)Si-NTs1.0 ≈ *7.0*PW_{12}/ZrO_2-Si(Et)Si-NTs1.0 > *14.8*PW_{12}/ZrO_2-Si(Et)Si-NTs1.0 > *3.7*PW_{12}/ZrO_2-Si(Et)Si-NTs1.0. That is, after the reaction is carried out for 60 min, the yield of methyl levulinate reaches 99.9, 99.7, 95.6, and 86.0%, respectively, for the *12.1*PW_{12}/ZrO_2-Si(Et)Si-NTs1.0-, *7.0*PW_{12}/ZrO_2-Si(Et)Si-NTs1.0-, *14.8*PW_{12}/ZrO_2-Si(Et)Si-NTs1.0-, and *3.7*PW_{12}/ZrO_2-Si(Et)Si-NTs1.0-catalyzed esterification reactions. Since the four tested nanohybrids have the same tubular nanostructure, the lower catalytic activity of *14.8*PW_{12}/ZrO_2-Si(Et)Si-NTs1.0 or *3.7*PW_{12}/ZrO_2-Si(Et)Si-NTs1.0 is due to its smaller BET surface area (198 $m^2 g^{-1}$) or lower Brønsted acid site density (2231 μeq g^{-1}).

Next, the most active *12.1*PW_{12}/ZrO_2-Si(Et)Si-NTs1.0 is also applied in esterification of levulinic acid with ethanol and *n*-butanol to produce ethyl levulinate and *n*-butyl levulinate. From the results shown in Fig. 7 it is found that *12.1*PW_{12}/ZrO_2-Si(Et)Si-NTs1.0 still exhibits quite high catalytic activity in the synthesis of ethyl levulinate and *n*-butyl levulinate, and the corresponding yield is 74.8 (ethyl levulinate) and 69.6% (*n*-butyl levulinate), respectively, after the reaction proceeds for 60 min. Influence of various alcohols on the esterification reactions is explained in terms of polarity and steric hindrance of the reaction substrate. On one hand, various alcohols are both reactant and solvents. With the polarity of alcohols decreasing from methanol to *n*-butanol, the miscibility of levulinic acid with the corresponding alcohol is lower, leading to a decreased esterification reaction rate, since the esterification reaction rate is controlled by the mass transfer rate between the two phases [45]. On the other hand, the nucleophilic attack of the protonated levulinic acid by the hydroxyl group of alcohol is the rate-determining step of the esterification reaction [30]. With increasing length of the carbon chain of the alcohol, steric hindrance occurs on the hydroxyl of the alcohol, which probably reduces the efficient nucleophilic attack of the hydroxyl group to the protonated carbonyl carbon of levulinic acid.

Finally, at a similar $H_3PW_{12}O_{40}$ loading (12.1–12.7 wt.%), the catalytic activity of the *12.1*PW_{12}/ZrO_2-Si(Et)Si-NTs1.0 is further compared with its 2D hexagonal *p6mm* mesostructured counterpart (*12.2*PW_{12}/ZrO_2-Si(Et)Si-$2D_{hex}$1.0), bridging ethyl group-free 2D hexagonal *p6mm* mesostructured nanohybrid (*12.1*PW_{12}/ZrO_2-SiO_2-$2D_{hex}$1.0), and silica-free nanohybrid (*12.7*PW_{12}/ZrO_2); additionally, commercially available solid acid, Amberlyst-15, is also tested under the same conditions. From the results presented in Fig. 8a it is found that the tested catalysts follow the activity order *12.1*PW_{12}/ZrO_2-Si(Et)Si-NTs1.0 > *12.2*PW_{12}/ZrO_2-Si(Et)Si-$2D_{hex}$1.0 > *12.1*PW_{12}/ZrO_2-SiO_2-$2D_{hex}$1.0 > *12.7*PW_{12}/ZrO_2 > Amberlyst-15. For example, after the esterification reaction proceeds for 60 min, the yield of methyl levulinate reaches 99.9, 81.6, 79.4, 70.6, and 58.8%, respectively, for the *12.1*PW_{12}/ZrO_2-Si(Et)Si-NTs1.0-, *12.2*PW_{12}/ZrO_2-Si(Et)Si-$2D_{hex}$1 .0-, *12.1*PW_{12}/ZrO_2-SiO_2-$2D_{hex}$1.0-, *12.7*PW_{12}/ZrO_2-, and Amberlyst-15-catalyzed esterification reactions. When the reaction time is increased further to 90 min, the yield of methyl levulinate approaches 100% for the *12.1*PW_{12}/ZrO_2-Si(Et)Si-NTs1.0-, *12.2*PW_{12}/ZrO_2-Si(Et)Si-$2D_{hex}$1.0-, and *12.1*PW_{12}/ZrO_2-SiO_2-$2D_{hex}$1.0-catalyzed esterification reactions. Since these acid catalysts possess different acid site densities, their esterification activities are further compared in terms of the yield of methyl levulinate per acid site of each catalyst (TOF, h^{-1}) at 30 min. From the results shown in Fig. 8b it is found that the tested catalysts follow

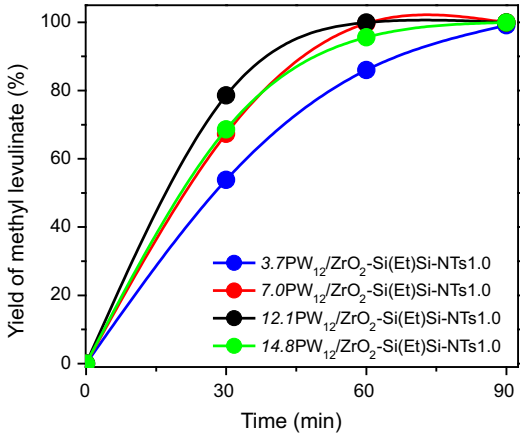

Fig. 6. Influence of $H_3PW_{12}O_{40}$ loading on the catalytic activity of the tubular PW_{12}/ZrO_2-Si(Et)Si nanohybrids in esterification of levulinic acid (12.44 mmol) with methanol (87.08 mmol) to yield methyl levulinate: 2 wt.% catalyst, 65 °C, atmospheric pressure.

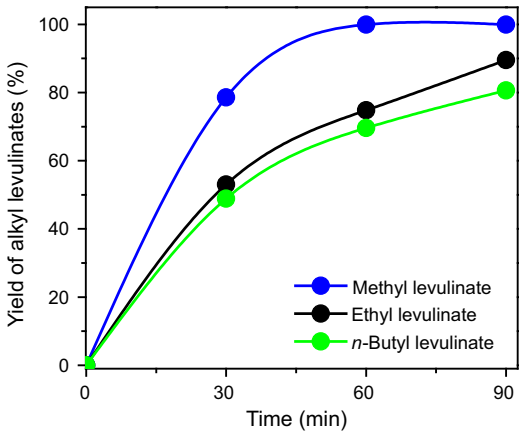

Fig. 7. Catalytic activity of the *12.1*PW_{12}/ZrO_2-Si(Et)Si-NTs1.0-catalyzed esterification of levulinic acid (12.44 mmol) with methanol, ethanol, or *n*-butanol (87.08 mmol) to yield methyl levulinate, ethyl levulinate, or *n*-butyl levulinate: 2 wt.% catalyst, refluxing temperature, atmospheric pressure.

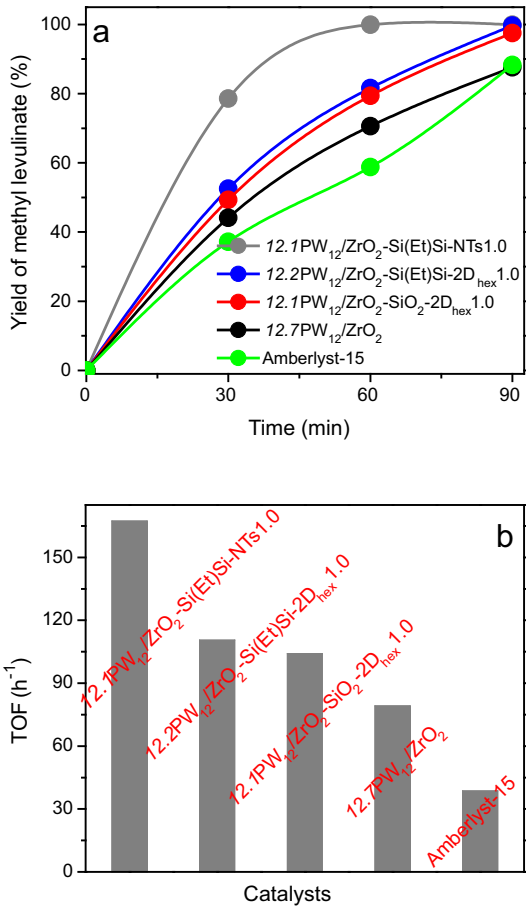

Fig. 8. Catalytic activity comparison of various PW_{12}/ZrO_2-based hybrid nanocatalysts in esterification of levulinic acid (12.44 mmol) with methanol (87.08 mmol) to yield methyl levulinate (a) and the yield of methyl levulinate per acid site (TOF, h^{-1}) at 30 min (b): 2 wt.% catalyst, 65 °C, atmospheric pressure. Commercially available Amberlyst-15 was also tested.

the TOF order *12.1*PW_{12}/ZrO_2-Si(Et)Si-NTs1.0 (167.3 h^{-1}) > *12.2*PW_{12}/ZrO_2-Si(Et)Si-2D_{hex}1.0 (110.5 h^{-1}) > *12.1*P W_{12}/ZrO_2-SiO_2-2D_{hex}1.0 (104.1 h^{-1}) > *12.7*PW_{12}/ZrO_2 (79.2 h^{-1}) > Amberlyst-15 (38.6 h^{-1}). Although the *12.2*PW_{12}/ZrO_2-Si(Et)Si-2D_{hex}1.0 nanohybrid has a larger BET surface area (346 $m^2\ g^{-1}$) than its tubular counterpart (243 $m^2\ g^{-1}$), its lengthened diffusion path owing to longer pore channels can extend the diffusion path. Thus, the reactant/product diffusion and mass transfer are slowed down to some extent, leading to lower esterification activity than for its tubular counterpart. In the case of bridging ethyl group-free *12.1*PW_{12}/ZrO_2-SiO_2-2D_{hex}1.0, its slightly lower activity than that of *12.1*PW_{12}/ZrO_2-Si(Et)Si-NTs1.0 may be due to its hydrophilic surface. In the case of *12.7*PW_{12}/ZrO_2, its poor porosity, including smaller BET surface area (138 $m^2\ g^{-1}$) and lower pore volume (0.11 $cm^3\ g^{-1}$) as well as its disordered mesostructure, lead to its having the lowest esterification activity among the four tested PW_{12}/ZrO_2-based hybrid nanocatalysts. As for the reference solid acid catalyst, Amberlyst-15, although it has extremely high acid site density (4800 μeq g^{-1}, [46]), its small BET surface area (50 $m^2\ g^{-1}$) and poor accessibility of the acid sites gives it the lowest esterification activity.

3.2.2. Ethanolysis of furfuryl alcohol

To expand the scope of their applications, the heterogeneous acid catalytic activity of the *12.1*PW_{12}/ZrO_2-Si(Et)Si-NTs1.0 nanohybrid is further tested in ethanolysis of furfuryl alcohol to yield ethyl levulinate under the conditions of furfuryl alcohol-to-ethanol molar ratio 1:60, 1.5 wt.% solid catalyst, and 120 °C (Scheme 3); additionally, its catalytic activity is also compared with some reference homogeneous (e.g., $H_3PW_{12}O_{40}$ and HCl) and heterogeneous (e.g., $Cs_{2.5}H_{0.5}PW_{12}O_{40}$ and Amberlyst-15) acid catalysts. Fig. 9a displays the catalytic activity of the tested catalysts expressed by the yield of ethyl levulinate, showing that they follow the activity order HCl > Amberlyst-15 > $H_3PW_{12}O_{40}$ > *12.1*PW_{12}/ZrO_2-Si(Et)Si-NTs1.0 > $Cs_{2.5}H_{0.5}PW_{12}O_{40}$. For the HCl-, Amberlyst-15-, $H_3PW_{12}O_{40}$-, *12.1*PW_{12}/ZrO_2-Si(Et)Si-NTs1.0-, and $Cs_{2.5}H_{0.5}PW_{12}O_{40}$-catalyzed ethanolysis reactions, the yield of ethyl levulinate reaches 82.0, 57.4, 55.2, 32.1, and 8.1%, respectively, after the reaction proceeds for 30 min. When the reaction time is further increased to 180 min, the yield of ethyl levulinate approaches 92.3, 89.2, 70.2, 69.8, and 28.7% for the Amberlyst-15-, HCl-, $H_3PW_{12}O_{40}$-, *12.1*PW_{12}/ZrO_2-Si(Et)Si-NTs1.0-, and $Cs_{2.5}H_{0.5}PW_{12}O_{40}$-catalyzed ethanolysis reactions. Since these acid catalysts possess different acid site densities, their ethanolysis activity is further compared in terms of the yield of ethyl levulinate per acid site of each catalyst (TOF, h^{-1}) at 10 min. From the results shown in Fig. 9b, it is found that the tested catalysts follow the TOF order $H_3PW_{12}O_{40}$ (22.4 h^{-1}) > $Cs_{2.5}H_{0.5}PW_{12}O_{40}$ (21.2 h^{-1}) > *12.1*PW_{12}/ZrO_2-Si(Et)Si-NTs1.0 (7.2 h^{-1}) > Amberlyst-15 (5.6 h^{-1}) > HCl (1.8 h^{-1}). Although $Cs_{2.5}H_{0.5}PW_{12}O_{40}$ and $H_3PW_{12}O_{40}$ show higher TOF value than *12.1*PW_{12}/ZrO_2-Si(Et)Si-NTs1.0 in the ethanolysis reaction, $Cs_{2.5}H_{0.5}PW_{12}O_{40}$ can form a milky dispersion in the reaction media, while $H_3PW_{12}O_{40}$ dissolves in the reaction media. Both cases lead to difficult separation of the catalyst for recycling uses, and there-

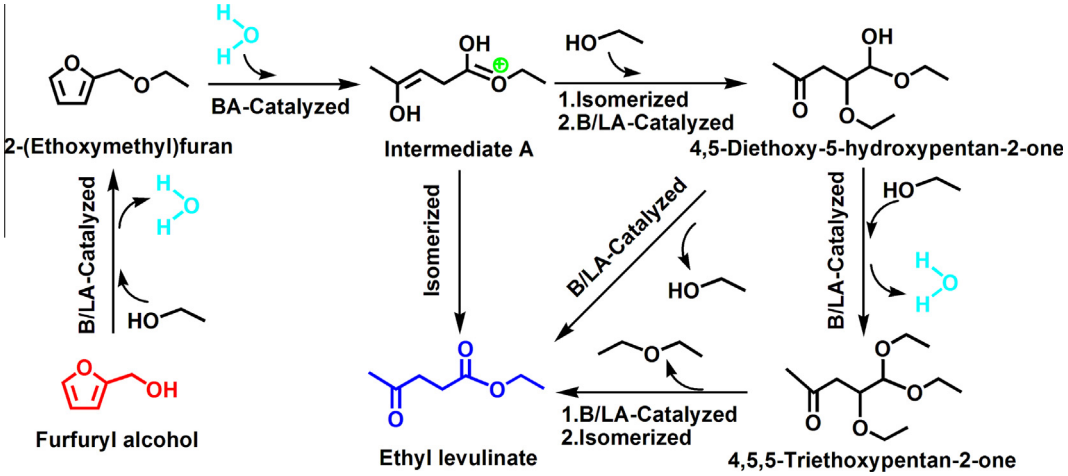

Scheme 3. Possible reaction mechanism for the alcoholysis of furfuryl alcohol to produce ethyl levulinate catalyzed over the PW_{12}/ZrO_2-Si(Et)Si-NTs nanohybrids.

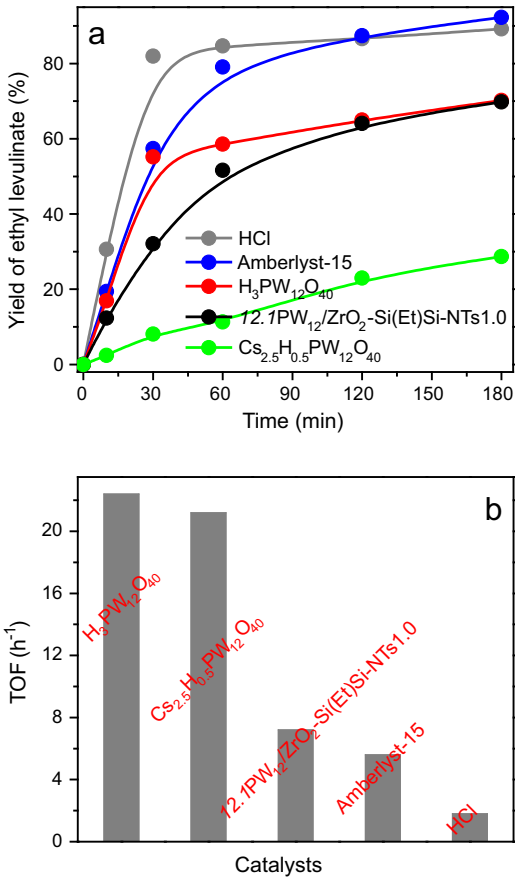

Fig. 9. Catalytic activity comparison of the *12.1*PW_{12}/ZrO_2-Si(Et)Si-NTs1.0 with some reference acid catalysts toward ethanolysis of furfuryl alcohol in terms of the yield of ethyl levulinate (a) and the yield of ethyl levulinate per acid site (TOF, h^{-1}) at 10 min (b): furfuryl alcohol 1.15 mmol, ethanol 69.00 mmol, 1.5 wt.% solid acid catalyst or 1.2 mmol HCl solution, 120 °C.

fore they are not competitive with heterogeneous acid catalysts from the viewpoint of practical applications.

In current work, the PW_{12}/ZrO_2-Si(Et)Si-catalyzed esterification reaction is performed under conditions of atmospheric refluxing and higher alcohol-to-levulinic acid molar ratio (7:1), and the selectivity of the catalyst to alkyl levulinates can reach 100%. However, differently from the esterification reaction, the present ethanolysis reaction is carried out under solvothermal conditions (120 °C), and the intermediates and byproducts are produced inevitably, which limits the selectivity to ethyl levulinate as well as the yield of ethyl levulinate. GC–MS is therefore applied to identify these compounds (Fig. S4 and Table S1 of the electronic Supplementary Information). The intermediates identified are 2-(ethoxymethyl)furan (main), 4,5-diethoxy-5-hydroxypentan-2-one (minor), and 4,5,5-triethoxypentan-2-one (minor), while the byproducts found are diethyl ether (nonproductive consumption of ethanol) and some oligomeric products of furfuryl alcohol such as difuran-2-ylmethane, 2-[(furan-2-ylmethoxy)methyl]furan, and 2,5-bis(furan-2-ylmethyl)furan (Table S1 of the electronic Supplementary Information). Formation of these oligomeric products results in the original white catalyst powder turning dark after the reaction and remaining this color after dichloromethane washing. Introduction of hydrophobic ethyl groups into the PW_{12}/ZrO_2 framework can enhance the surface hydrophobicity of the hybrid catalysts, and therefore the adsorption of the oligomeric products on the catalyst surface is inhibited to some degree, leading to the regeneration of the catalysts more easily (see Section 3.2.4).

The selectivity of the *12.1*PW_{12}/ZrO_2-Si(Et)Si-NTs1.0 to ethyl levulinate and 2-(ethoxymethyl)furan at different reaction times (30, 60, 120, and 180 min) is summarized in Table S2 of the electronic Supplementary Information. The selectivity to ethyl levulinate increases with the reaction time, while the selectivity to 2-(ethoxymethyl)furan gradually decreases with the reaction time. It should be mentioned that conversion of furfuryl alcohol reaches nearly 100% after the reaction proceeds for 30 min at 120 °C.

3.2.3. Possible reaction mechanism and influence of water

The mechanism of the Brønsted or Lewis acid-catalyzed esterification reaction has been studied by Melero's groups [47], and it is possible to infer a similar mechanism of esterification of levulinic acid with alcohol catalyzed by the PW_{12}/ZrO_2-Si(Et)Si-NTs nanohybrids with Brønsted and Lewis double acid sites (Scheme 2a). On one hand, the strong Brønsted acid sites can protonate carbonyl groups of levulinic acid molecules in the first step of the esterification reaction (the upper portion of Scheme 2a), which gives oxonium ions that are readily attacked by alcohol molecules through an exchange reaction to produce alkyl levulinate molecules after losing one hydrogen atom. On the other hand, direct coordination of levulinic acid with unsaturated surface Zr^{4+} sites is the first step in the Lewis acid-catalyzed esterification reactions (the bottom portion of Scheme 2a). In the second and third steps, they follow the same procedures as those of the Brønsted acid-catalyzed esterification reactions. Esterification is a reversible process, and water is the byproduct of the esterification reaction. Therefore, the surface hydrophobicity of solid acid catalysts becomes important for heterogeneous acid-catalyzed esterification reactions. To investigate the effect of water on esterification, the experiments are carried out by adding some excess water (5.56 mmol) in reaction media under the conditions levulinic acid-to-methanol molar ratio 1:7, 2 wt.% catalyst, 65 °C, and atmospheric pressure. The catalytic activity of as-prepared *12.1*PW_{12}/ZrO_2-Si(Et)Si-NTs1.0 and *12.1*PW_{12}/ZrO_2-SiO_2-2D_{hex}1.0 hybrid catalysts is compared (Fig. 10a and b). The reaction rates of two tested catalysts both significantly decreased after the addition of 5.56 mmol water into the initial reaction system. Since esterification is an equilibrium reaction, the presence of water from the beginning of the reaction could inhibit the progress of the formation of esters. However, in the *12.1*PW_{12}/ZrO_2-Si(Et)Si-NTs1.0-catalyzed esterification of levulinic acid with methanol containing excess water, the yield of methyl levulinate reaches 97.4% after the reaction proceeds for 90 min, which is similar to that in the water-free system (Fig. 10a). One important reason is that methanol is used in excess; moreover, the surface hydrophobicity of the *12.1*PW_{12}/ZrO_2-Si(Et)Si-NTs1.0 hybrid catalyst can effectively prevent water molecules from remaining in the acid sites and avoid the poisoning of the acid sites. As for the ethyl-group-free *12.1*PW_{12}/ZrO_2-SiO_2-2D_{hex}1.0 hybrid catalyst, it exhibits obviously lower catalytic activity in the presence of 5.56 mmol water compared with the water-free system, and the yield of methyl levulinate only reaches 63.9% (Fig. 10b). Consequently, it is confirmed that the surface hydrophobicity of the solid acid catalyst plays an important role in maintaining its esterification activity in the presence of water in the reaction medium.

The mechanism of ethanolysis of furfuryl alcohol catalyzed by PW_{12}/ZrO_2-Si(Et)Si-NTs is put forward based on the literature [48,49] as well as the identified intermediates in the current reaction system, which is illustrated in Scheme 2b. Similarly to the first step in the esterification reaction, the furfuryl alcohol molecules are first activated by the Brønsted and Lewis acid sites of the hybrid catalysts, and the activated furfuryl alcohol molecules are attacked by ethanol molecules to form 2-(ethoxymethyl)furan and water molecules. Next, the intermediate A is formed via the ring-opening reaction owing to water molecules attacking cyclic oxonium obtained by protonation of epoxy groups in the presence of Brønsted acid sites.

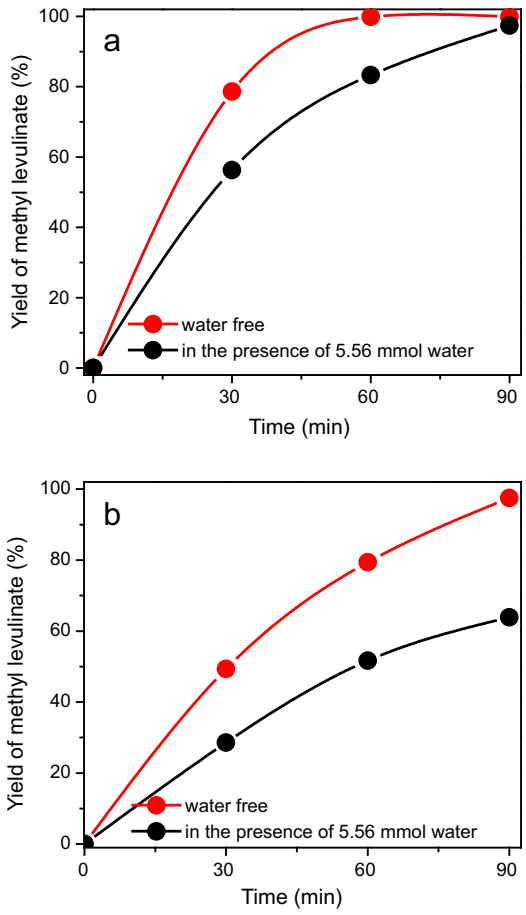

Fig. 10. Influence of extra water on the esterification activity of *12.1*PW_{12}/ZrO_2-Si(Et)Si-NTs1.0 (a) and *12.1*PW_{12}/ZrO_2-SiO_2-$2D_{hex}$1.0 (b): levulinic acid 12.44 mmol, methanol 87.08 mmol, 2 wt.% catalyst, 90 min, 65 °C, atmospheric pressure.

Subsequently, the formation of ethyl levulinate may undergo the following possible approaches: (i) The intermediate A is isomerized, together with releasing one hydrogen atom, and ethyl levulinate is formed. (ii) The intermediate A is isomerized, and the produced compound is activated by the Brønsted and Lewis acid sites. After being attacked by ethanol molecules, 4,5-diethoxy-5-hydroxype ntan-2-one is formed. Further being attacked by ethanol molecules, 4,5,5-triethoxypentan-2-one is formed, together with the release of water molecules. After release of one diethyl ether molecule from 4,5,5-triethoxypentan-2-one followed by isomerization, ethyl levulinate is formed. (iii) After release of one ethanol molecular from 4,5-diethoxy-5-hydroxypentan-2-one followed by isomerization, ethyl levulinate is formed.

To investigate the influence of water on the ethanolysis activity of *12.1*PW_{12}/ZrO_2-Si(Et)Si-NTs1.0, the experiments are carried out by adding some excess water (5.56 mmol) to the reaction media under the conditions of furfuryl alcohol-to-ethanol molar ratio 1:60 and 120 °C. Fig. 11a displays the yield of ethyl levulinate vs. reaction time, showing that the activity increases slightly in the presence of 5.56 mmol water with respect to the water-free system. That is, after the reaction proceeds for 3 h, the yield of ethyl levulinate is 69.8% (water-free system) and 74.3% (in the presence of 5.56 mmol water), respectively. From consideration of the above mechanism it is found that the presence of water can facilitate the formation of ethyl levulinate via ethanolysis of furfuryl alcohol and thus a few extra water molecules in the reaction system can have a positive influence on the *12.1*PW_{12}/ZrO_2-Si(Et)Si-NTs1.0-catalyzed synthesis of ethyl levulinate. Additionally, the surface hydrophobicity of the *12.1*PW_{12}/ZrO_2-Si(Et)Si-NTs1.0 not only can separate water molecules from the acid sites to avoid deactivation, but also effectively reduce the absorption of oligomeric products, which is critical for maintaining the catalytic activity in the reaction system containing a small amount of water.

Fig. 11b shows the yield of 2-(ethoxymethyl)furan vs. reaction time. 2-(Ethoxymethyl)furan is the main intermediate of ethanolysis of furfuryl alcohol, and conversion of furfuryl alcohol into 2-(ethoxymethyl)furan is a fast step. With increasing reaction time, the yield of 2-(ethoxymethyl)furan decreases gradually. That is, after the reaction proceeds for 1, 2, and 3 h, the yield of 2-(ethoxymethyl)furan reaches 27.8, 17.6, and 12.6%, respectively, in the water-free system, indicating that it is transferred into ethyl levulinate rapidly. A similar trend can be found in the system containing 5.56 mmol water; however, the yield of 2-(ethoxymethyl) furan decreases significantly compared with that in a water-free system, and after the reaction proceeds for 3 h, the yield of 2-(ethoxymethyl)furan is 6.6%. The result may be due to the following two reasons: (i) excessive water can inhibit the formation of 2-(ethoxymethyl)furan to some extent, since water is released during the conversion of furfuryl alcohol to 2-(ethoxymethyl) furan; and (ii) further addition of water can accelerate ring-opening of 2-(ethoxymethyl)furan.

3.2.4. Regeneration and reusability

The reusability of the heterogeneous catalyst in a liquid medium is an outstanding advantage. Here, the reusability of *12.1*PW_{12}/ZrO_2-Si(Et)Si-NTs1.0 is evaluated in both esterification

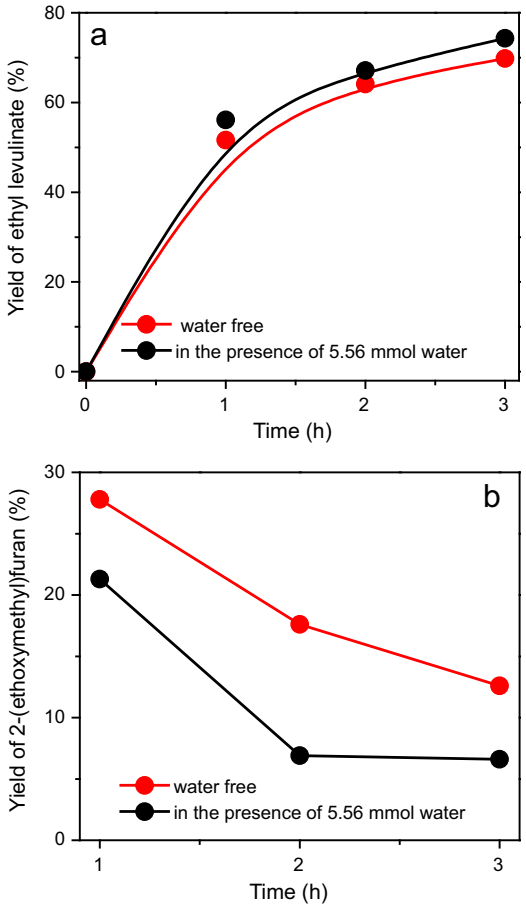

Fig. 11. Influence of extra water on the alcoholysis activity of *12.1*PW_{12}/ZrO_2-Si(Et)Si-NTs1.0 in terms of the yield of ethyl levulinate (a) and 2-(ethoxymethyl)furan (b): furfuryl alcohol 1.15 mmol, ethanol 69.00 mmol, 1.5 wt.% catalyst, 120 °C.

and ethanolysis reactions. After each catalytic cycle, the hybrid catalyst is recovered by centrifugation, and then it is washed three times with dichloromethane. After being dried at 100 °C overnight, the hybrid nanocatalyst is weighed and applied to the second and third cycles under the same conditions. As shown in Fig. 12a, the esterification activity of the spent and fresh catalysts is almost the same; e.g., after the reaction performs for 60 min, the yield of methyl levulinate is 99.9% (the first cycle), 97.2% (the second cycle), and 99.9% (the third cycle), respectively. The result clearly demonstrates high esterification stability of the *12.1*PW_{12}/ZrO_2-Si(Et)Si-NTs1.0 hybrid nanocatalyst. This high esterification stability is attributed to (i) the strong covalent bonding between the Keggin units and ZrO_2 framework, which can effectively prevent the Keggin units from leaching into the reaction medium; and (ii) the surface hydrophobicity of the catalyst, which can inhibit the strong adsorption of the yielded water molecule.

However, for the ethanolysis of furfuryl alcohol, after the first catalytic cycle, the catalytic activity of the spent catalyst decreases slightly compared with that of the fresh one, and then it is almost unchangeable. That is, after the reaction is performed for 120 min, the yield of ethyl levulinate is 64.1% (the first cycle), 53.7% (the second cycle), and 53.0% (the third cycle), respectively (Fig. 12b). Through monitoring the concentration of P and W in the catalyst powder-free reaction solutions by ICP-AES, it is found that the leaching of the Keggin units is negligible. Therefore, it is inferred that the activity loss of the catalyst after the first catalytic cycle is due to the adsorption of some oligomeric byproducts on the surface of *12.1*PW_{12}/ZrO_2-Si(Et)Si-NTs1.0, which may decrease the accessibility of the acid sites to the reactants, although the introduction of hydrophobic ethyl groups into the framework of the hybrid catalyst can increase the surface hydrophobicity to some extent. Additionally, the oligomeric byproduct-adsorbed catalyst can inhibit further absorption of oligomeric products on the catalyst surface, which results in the catalytic activity of the third spent catalyst remaining unchangeable.

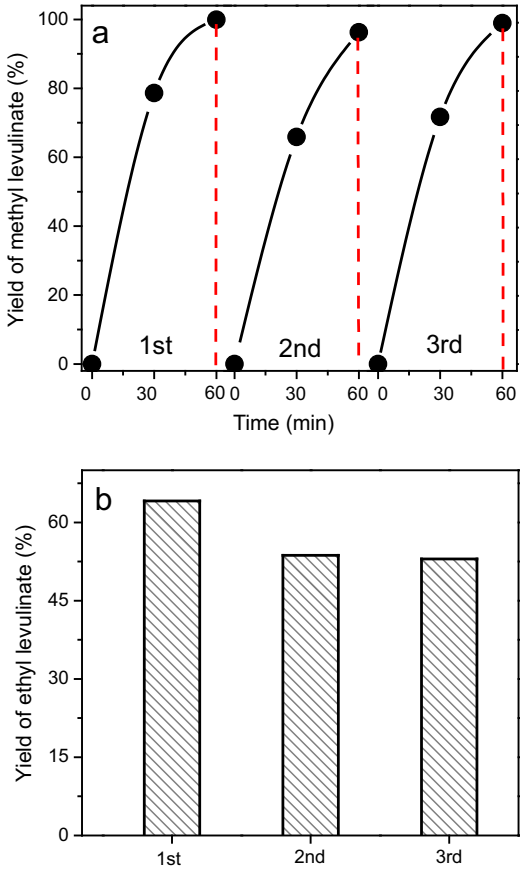

Fig. 12. Reusability of the *12.1*PW_{12}/ZrO_2-Si(Et)Si-NTs1.0 toward esterification of levulinic acid with methanol (a) and ethanolysis of furfuryl alcohol with ethanol (b). Conditions for esterification reaction: levulinic acid 12.44 mmol, methanol 87.08 mmol, 2 wt.% catalyst, 1 h, 65 °C, atmospheric pressure. Conditions for ethanolysis reaction: furfuryl alcohol 1.15 mmol, ethanol 69.00 mmol, 1.5 wt.% catalysts, 2 h, 120 °C.

4. Conclusions

A novel environmentally friendly solid acid catalyst, Keggin type heteropoly acid and ZrO_2 bifunctionalized organosilica nanotubes (PW_{12}/ZrO_2-Si(Et)Si-NTs), was successfully prepared by a P123 single-micelle-templated sol–gel co-condensation route. By changing the Si-to-Zr molar ratio and acidity in the initial gel mixture, the hydrolysis/condensation rate and hydrophobicity/hydrophilicity of the bisilylated organic precursor and zirconium *n*-butoxide precursor were adjusted, which played the key role in fabricating PW_{12}/ZrO_2-Si(Et)Si hybrid nanocatalysts with a 1D hollow tubular nanostructure. The PW_{12}/ZrO_2-Si(Et)Si-NTs showed excellent heterogeneous acid catalytic activity toward synthesis of alkyl levulinates from esterification of levulinic acid and ethanolysis of furfuryl alcohol, attributed to: (i) strong Brønsted and Lewis acidity of the hybrid nanocatalysts, which played a dominant role in the catalytic activity; (ii) 1D hollow tubular morphology with extremely thin walls and accessible mesochannels, which could shorten the diffusion path and facilitate mass transfer, so that improved accessibility of the acid sites to the reactant molecules was obtained; and (iii) hydrophobic surface owing to the introduction of ethane-bridged organosilica units, which can inhibit the strong adsorption of the hydrophilic byproducts. Additionally, combining strong interaction between the Keggin units with ZrO_2 and surface hydrophobicity, the PW_{12}/ZrO_2-Si(Et)Si-NTs exhibited good reusability in both target reactions, showing the potential for application in synthesis of alkyl levulinates from biomass-derived platform molecules.

Acknowledgments

This work is supported by the Natural Science Fund Council of China (21173036; 21573038; 51008056).

Appendix A. Supplementary material

Supplementary data associated with this article can be found, in the online version, at http://dx.doi.org/10.1016/j.jcat.2015.10.018.

References

[1] R.K. Sharma, S. Sharma, S. Dutta, R. Zboril, M.B. Gawande, Green Chem. 17 (2015) 3207–3230.
[2] M.M. Antunes, S. Lima, P. Neves, A.L. Magalhaes, E. Fazio, A. Fernandes, F. Neri, C.M. Silva, S.M. Rocha, M.F. Ribeiro, M. Pillinger, A. Urakawa, A.A. Valente, J. Catal. 329 (2015) 522–537.
[3] J. Dhainaut, J.P. Dacquin, A.F. Lee, K. Wilson, Green Chem. 12 (2010) 296–303.
[4] J. Du, X.Y. Lai, N.L. Yang, J. Zhai, D. Kisailus, F.B. Su, D. Wang, L. Jiang, ACS Nano 5 (2011) 590–596.
[5] C.C. Li, J. Dou, L.W. Chen, J.Y. Lin, H.C. Zeng, ChemCatChem 4 (2012) 1675–1682.
[6] L. Qin, X.X. Pan, L. Wang, X.P. Sun, G.L. Zhang, X.W. Guo, Appl. Catal., B: Environ. 150–151 (2014) 544–553.
[7] X. Zhang, H.X. Chen, Y.P. Xie, J.X. Guo, J. Mater. Chem. A 2 (2014) 3912–3918.
[8] S.T. Oyama, X. Zhang, J. Lu, Y. Gud, T. Fujitani, J. Catal. 257 (2008) 1–4.
[9] P. Bui, J.A. Cecilia, S.T. Oyama, A. Takagaki, A. Infantes-Molina, H. Zhao, D. Li, E. Rodríguez-Castellón, A.J. López, J. Catal. 294 (2012) 184–198.
[10] X. Liu, X.B. Li, Z.H. Guan, J. Liu, J. Zhao, Y. Yang, Q.H. Yang, Chem. Commun. 47 (2011) 8073–8075.
[11] J.A. Melero, R. Grieken, G. Morales, Chem. Rev. 106 (2006) 3790–3812.
[12] F. Su, Y.H. Guo, Green Chem. 16 (2014) 2934–2957.

[13] G.M. Ziarani, A.R. Badiei, M. Azizi, Sci. Iran. 18 (2011) 453–457.
[14] T.M. Suzuki, T. Nakamura, E. Sudo, Y. Akimoto, K. Yano, Microporous Mesoporous Mater. 111 (2008) 350–358.
[15] M.I. López, D. Esquivel, C. Jiménez-Sanchidrián, F.J. Romero-Salguero, P.V.D. Voort, J. Catal. 326 (2015) 139–148.
[16] B. Lu, S. An, D.Y. Song, F. Su, X. Yang, Y.H. Guo, Green Chem. 17 (2015) 1767–1778.
[17] X.H. Zhang, F. Su, D.Y. Song, S. An, B. Lu, Y.H. Guo, Appl. Catal., B: Environ. 163 (2015) 50–62.
[18] S. An, D.Y. Song, B. Lu, X. Yang, Y.H. Guo, Chem. Eur. J. 21 (2015) 10786–10798.
[19] F. Su, S. An, D.Y. Song, X.H. Zhang, B. Lu, Y.H. Guo, J. Mater. Chem. A 2 (2014) 14127–14138.
[20] G. Pasquale, P. Vázquez, G. Romanelli, G. Baronetti, Catal. Commun. 18 (2012) 115–120.
[21] Z.H. Zhang, K. Dong, Z.B. Zhao, ChemSusChem 4 (2011) 112–118.
[22] M. Kuzminska, T.V. Kovalchuk, R. Backov, E.M. Gaigneaux, J. Catal. 320 (2014) 1–8.
[23] K. Srilatha, T. Issariyakul, N. Lingaiah, P.S.S. Prasad, J. Kozinski, A.K. Dalai, Energy Fuels 24 (2010) 4748–4755.
[24] G.S. Armatas, G. Bilis, M. Louloudi, J. Mater. Chem. 21 (2011) 2997–3005.
[25] A.M. Alsalme, P.V. Wiper, Y.Z. Khimyak, E.F. Kozhevnikova, I.V. Kozhevikov, J. Catal. 276 (2010) 181–189.
[26] B. Samaranch, P.R. Piscina, G. Clet, M. Houalla, P. Gélin, N. Homs, Chem. Mater. 19 (2007) 1445–1451.
[27] T. Rajkumar, G. Ranga Rao, J. Mol. Catal. A: Chem. 295 (2008) 1–9.
[28] E. López-Salinas, J.G. Hernández-Cortéz, I. Schifter, E. Torres-García, J. Navarrete, A. Gutiérrez-Carrillo, T. López, P.P. Lottici, D. Bersani, Appl. Catal., A: Gen. 193 (2000) 215–225.
[29] K. Jacobson, R. Gopinath, L.C. Meher, A.K. Dalai, Appl. Catal., B: Environ. 85 (2008) 86–91.
[30] F. Su, Q.Y. Wu, D.Y. Song, X.H. Zhang, M. Wang, Y.H. Guo, J. Mater. Chem. A 1 (2013) 13209–13221.
[31] R. Le Van Mao, Q. Zhao, G. Dima, D. Petraccone, Catal. Lett. 141 (2011) 271–276.
[32] A. Demolis, N. Essayem, F. Rataboul, A.C.S. Sust, Chem. Eng. 2 (2014) 1338–1352.
[33] L. Hu, G. Zhao, W. Hao, X. Tang, Y. Sun, L. Lin, S. Liu, RSC Adv. 2 (2012) 11184–11206.
[34] A.A. Kiss, A.C. Dimian, G. Rothenberg, Adv. Synth. Catal. 348 (2006) 75–81.
[35] P. Lanzafame, K. Barbera, S. Perathoner, G. Centi, A. Aloise, M. Migliori, A. Macario, J.B. Nagy, G. Giordano, J. Catal. 330 (2015) 558–568.
[36] M. Mandal, M. Kruk, Chem. Mater. 24 (2011) 123–132.
[37] I. Ogino, Y. Suzuki, S.R. Mukai, ACS Catal. 5 (2015) 4951–4958.
[38] L.L. Xu, Y.H. Wang, X. Yang, X.D. Yu, Y.H. Guo, J.H. Clark, Green Chem. 10 (2008) 746–755.
[39] B. Liu, R.T. Baker, J. Mater. Chem. 18 (2008) 5200–5207.
[40] C.W. Young, P.C. Servais, C.C. Currie, M.J. Hunter, J. Am. Chem. Soc. 70 (1948) 3758–3764.
[41] M.H. Tucker, A.J. Crisci, B.N. Wigington, N. Phadke, R. Alamillo, J. Zhang, S.L. Scott, J.A. Dumesic, ACS Catal. 2 (2012) 1865–1876.
[42] F. Su, L. Ma, D.Y. Song, X.H. Zhang, Y.H. Guo, Green Chem. 15 (2013) 885–890.
[43] J. Liu, S.Y. Bai, H. Zhong, C. Li, Q.H. Yang, J. Phys. Chem. C 114 (2010) 953–961.
[44] M.G. Kulkarni, R. Gopinath, L.C. Meher, A.K. Dalai, Green Chem. 8 (2006) 1056–1062.
[45] A. Alegría, Á.L. Fuentes de Arriba, J.R. Morán, J. Cuellar, Appl. Catal., B: Environ. 160–161 (2014) 743–756.
[46] Y.B. Huang, Y. Fu, Green Chem. 15 (2013) 1095–1111.
[47] J.A. Melero, J. Iglesias, Gabriel morales, Green Chem. 11 (2009) 1285–1308.
[48] G.M.G. Maldonado, R.S. Assary, J.A. Dumesic, L.A. Curtiss, Energy Environ. Sci. 5 (2012) 8990–8997.
[49] G. Wang, Z. Zhang, L. Song, Green Chem. 16 (2014) 1436–1443.